O. E. Melnik[1,2*], I. S. Utkin[1], and I. N. Bindeman[3]

[1]Institute of Mechanics, Moscow State University, Moscow, Russia

[2]Fersman Mineralogical Museum, Russian Academy of Sciences, Moscow, Russia

[3]Department of Earth Sciences, University of Oregon, USA

*Corresponding author: Oleg Melnik (melnik@imec.msu.ru)

Paper is dedicated to late Alexander R. McBirney (1924-2019), renown volcanologist and a founder of the Volcanology Program in the University of Oregon

Word count:

Abstract – 249 words.

Text without Abstract and references but with figure captions: 10,000

Figures 15

Tables: 1

Key Points:

- A 2D model of magma chamber growth by dike injections shows that a vertically extended system of magma batches can be formed in a few ka
- Magma influx intensity and eruptions determine the size and location of pockets of melt
- Diffusion growth model with >10^5 particles links thermal evolution of a magma-host rock system with the behavior of zircon.

Abstract

We present a 2D model of magma body formation in granitic crust by injection of rhyolitic or basaltic dikes and sills. An elastic analytical solution enables computation of rock displacement in response to magma intrusion. Phase diagrams for magma and host rocks predict melting/crystallization. We combine this model with our zircon crystallization/dissolution software and compute zircon survival histories within individual batches of magma and country rocks.

Incremental accumulation of intruded magma generates interconnected magma batches of eruptible melt with melt fractions >50 vol% that form in clusters. The rate of melt production is highly variable in space and time. The volume of eruptible melt strongly depends on the input rates of magma Q and the width W of the injection region of dikes and on eruptions. For example, dikes injection with Q=0.125 m^3/s with W=5 km during 100 ka generates ~50 km^3 of eruptible melt while no significant melt forms if W=10 km. Injection of basaltic dikes produces more melt for the same flux rate. Frequent and small eruptions led to smaller magma bodies that are located deeper in the system, while systems with rare but voluminous eruption forms large melt.

Due to partial melting, most host rock zircons loose significant portion of their old cores and, thus, their average age is reduced. Magmatic zircons in the periphery of the intrusion form very quickly due to rapid dikes cooling while in its central part crystals contain old cores and young rims and can grow during several hundreds of ka.

Plain Language Summary

Formation of large magmatic eruptible bodies beneath active volcanoes or plutons in the Earth crust involves complicated thermo-mechanical processes related to magma injection, host rock melting, solid-melt separation, etc. Revealing enigmas requires joint efforts of geologist, geophysics and geomechanisists. With development of modern computer architecture and numerical methods modern models can capture details of these processes with increasing level of details. In this paper we present a new model of magma chamber formation based on intrusion of dikes and sills in 2D geometry with extremely high special resolution that can capture individual batches of injected magma. We use temperature-time histories recorded in more than 10,000 individual bathes of magma with zircon crystallization software previously published by us. We are now able to describe in detail magma chamber growth and formation, and link it to the history of zircon dissolution and growth.

1 Introduction

Magma body formation in the crust via intrusion and partial melting plays a fundamental role in the creation of the continental crust and has implications for volcanic hazard assessment. How much magma can be produced and stored in the crust under active volcanoes and caldera systems, its thermomechanical state, and the magmatic architecture of such magma systems are particularly critical to understanding magma body formation and longevity. The main mechanism of magma transport in the Earth's crust is via formation of cracks along which magma rises to the surface in the form of dikes and sills (Rubin, 1995). Basaltic magmas typically rise from mantle depths of several tens of kilometers carrying heat that enables a variety of melting phenomena in the crust (Huppert and Sparks, 1988; Annen and Sparks, 2002; Annen, 2009; Dufek and Bergantz, 2005). A common place of their generation revealed by geological and isotopic arguments (DePaolo et al, 2019), and thermomechanical modeling is in the lower crust or Moho (Colon et al. 2018), and this holds for a variety of tectonic environment ranging from plume to subduction zones. Differentiation products including basaltic andesites and andesites rise from these magmatic "hot zones" (e.g. Annen, 2009) in the lower crust and intrude the middle and upper crust in continental arc and intraplate systems, and pond in shallow magma bodies under volcanoes or calderas.

Dike widths can vary from centimeters to tens of meters and can extend laterally up to several hundred kilometers (Krumbholz et al., 2014). Both magma ascent and lateral dike propagation can achieve rates of meters per second and erupt many cubic kilometers of basalts in less than a year as is evidenced by histori-

cally observed eruptions such as Laki (15 km^3, Thordarsson and Self, 2003) and Bardarbunga (Gudmundsson et al. 2014), or Columbia River Basalts (Bindeman et al. 2020). Estimated magma flux rates range from 0.0001 km^3/yr in monogenetic magma fields in subduction-related environments to 0.1-1 km^3/yr in hot-spot volcanoes such as Hawaii (Robinson & Eakins, 2006), or during outbursts of magmatism such as those happening in Large Igneous Provinces (Costa et al. 2008; Bryan and Ernst, 2007).

High rates of magma injection generate significant overpressure in the upper crustal magma bodies, leading to volcanic eruptions (Caricchi et al., 2019). This gives a relatively narrow window of the influx rates and supply durations that can generate and accumulate large eruptible volume of magma suitable for super eruptions. The volcanic/plutonic ratio is an important and poorly constrained parameters in many magmatic systems; higher magma flux rates are thought to result in greater proportion of erupted materials, while low magma flux rate results in formation of plutons without a connection to the surface (e.g., Glazner et al. 2004).

Whether mantle-derived magma will erupt on the surface without much interaction with the crust, or stall in the crust, differentiate and cause crustal melting, is a century-old debate among petrologists, geophysicists, and modelers (Becerril et al. 2013; Edmonds et al., 2019 and references therein). Magma ascent in dikes is controlled primarily by the buoyancy forces and the tectonic stress field (Simakin and Talbott, 2001; Townsend et al. 2017). Most dikes do not reach the surface and are instead blocked at the level of neutral buoyancy (Walker, 1989), or with structural barriers in the form of stronger rock layers or melt zones (Edmonds et al. 2019). Repeated introduction of dikes into the near-surface (first kilometers) region of the Earth's crust leads to dike stalling and solidification, or upon repeated flow, formation of magma chambers with or without associated crustal melting (McBirney, 2006). As is evidenced from Large Igneous Provinces or supervolcanic eruptions, volumes of magma can reach thousands of cubic kilometers, although usually the volumes are much smaller (kilometers-tens of kilometers) and globally magmatic volumes vs. frequency follow typical log-linear relationships (Papale, 2018).

Magma chambers can be detected with some success by seismic tomography using shear wave attenuation (e.g., Heath et al., 2018). They may have an irregular shape, but most often appear to be flattened bodies with vertical or horizontal strike. The current paradigm is that there can be several chambers located at different depths under active volcanoes or caldera systems (Elsworth et al., 2014; Cashman et al., 2017), not very far from a textbook example of lower (hot zone) and upper crustal magma bodies in the crust (McBirney, 2006).

The numerical modeling of the formation of magma chambers by injection of magma in the crust started with a pioneering work of Huppert and Sparks (1988) who used 1D heat transfer model with realistic phase diagrams. In further development of these models, pseudo-2D and axisymmetric cylindrical coordinates were considered (Annen et al. 2006, Annen, 2009, Dufek and Bergantz, 2005).

Current modeling efforts proceed on all scales, but any given model is confined to either large regional processes or smaller scale local processes. On a regional scale, Colón et al. (2018, 2019) use the thermomechanical program of Gerya and Yuen (2003), which takes into consideration fully mechanically coupled crustal rheology, to simulate crust-wide multi-level magma system formation under the hot-spot environment of Yellowstone on million-year timescales. In more detailed local models, penetration and heat transfer between individual dikes and sills and host rocks are considered (Annen, 2009, Dufek & Bergantz, 2005). Models of the first type consider regions with a characteristic size of tens of kilometers and a grid spacing of several hundred meters. They cannot resolve the sub-grid heat exchange processes that occur during the transport of individual portions of magma, but they estimate the size and position of magma chambers based on the crust-upper mantle-wide distribution of temperatures, rheological properties of rocks and stresses, as well as the distribution of magma between individual chambers. In the models of the second type, the region in which magma is introduced is prescribed in advance based on the known geological structure of the crustal block, and available geochronological estimates of the time of formation of magmatic bodies. An example of the reconstruction of a real magmatic system of Jurassic Yerington batholith in Nevada is presented in (Schöpa et al., 2017). The model assumes horizontal sill emplacement with sinking of the underlying rock layers to accommodate the added mass, as in Annen et al., (2006). The heat equation is solved to account for the latent heat of melting for the host rocks and the real temperature dependence of the concentration of crystals in rocks and magma. An explicit scheme for solving the heat equation is used, which imposes a significant limitation on the time step and the total computational time. Biggs and Annen (2019) considered merging of two magmatic centers located at the same depth and corresponding ground deformation. They found that closely spaced intrusions can develop combined viscoelastic shells over time scales of 10s ka and form laterally extensive mush zones over time scales of 10–100 ka for the high melt supply rates and deep chambers where thermal conditions are suitable. Melt separation and migration is not considered in the model but should play significant role for lower magma fluxes.

In the model by Dufek & Bergantz, 2005, the introduction of dikes can appear in random directions within a certain crustal volume. To determine the field of displacements, the rocks are considered as a viscous fluid and the Naiver-Stokes equations are solved. However, this approach does not apply for low temperatures at which the behavior of the rocks is elastic. In (Karakas et al., 2017), the introduction of dikes is vertical. Each dike ends up with a sill at the top. Dike emplacements are stochastic in position and length. Rock movement is determined solely by kinematic relationships. Initially dikes are placed in the lower crust and lead to thermal maturation of the whole crustal body. Later the upper crustal reservoir is formed by dike injection into the upper crust. Simulations reveal that igneous provinces of less than a few hundred thousand years old are unlikely to support large upper crustal reservoirs, whereas longer-

lived systems (active for longer than 1 million years) can accumulate magma and build reservoirs capable of producing super-eruptions.

In all these models the efficiency of crustal melting defined as the volume of crustal melt produced by volume of deep magma injected is strongly dependent on the ambient temperature, (depth of the process), and the geothermal gradient (e.g., Colón et al. 2019). Melting starts after a period of heat incubation which is dependent on the flux rate. Furthermore, the efficiency of melting varies for different sill emplacement modes: underplating (when each subsequent sill is intruded under the previous), overplating, intraplating, and random intrusion into the sill-affected areas. Expectedly, efficiency of crustal melting and crustal melt productivity is decreasing in the listed order, because overplating delivers heat directly to the melting boundary and maintains the steep temperature gradient.

In the parallel effort by geologists, the lifetimes of individual magmatic systems, large and small, arc- or hotspot related, can be understood by the ever-improving U-Th-Pb geochronological methods involving single crystal zircon studies and most recently CA-ID-TIMS methods (e.g., Schaltegger et al. 2019). When considering young (<1-2 Ma) magmatic systems, resolution of individual magmatic episodes is possible on century timescales by considering zircon age spectra (Crowley et al. 2007). These recent studies demonstrated for example that silicic supereruptions with volume exceeding 1000 km^3 of eruptible magma can be generated in less than 5,000-10,000 years (which we call "Yellowstone" type), to longer than 500,000 years (which we call "Fish Canyon" type, e.g Bindeman and Simakin, 2014) based on concurrent CA-ID-TIMS efforts (Wotzlaw et al 2013, 2014, 2015). In the first case, the magma is a near-liquidus, crystal poor rhyolite, while in the second case erupted magma is a well-mixed near-solidus intermediate mush with 45% crystals (Bachmann et al. 2002). It is important to state that "cold and wet" arc magmatic system, the most abundant silicic magmatic factory on earth, exhibits a full spectrum of these behaviors, between these endmembers. Glazner et al. (2004) argued that given 10 Myr spread in ages of zircons in granites of the Tuolumne Intrusive Suite of Yosemite National Park, a major batholith in the Sierra Nevada Mountains (California) is formed by accumulation of silicic magmatic dikes and intrusions over similarly long and less robust magmatic episodes (also cf. Miller et al. 2011). These episodes may never have an active volcanic connection to the surface, and late-plutonic processes after such dike accretion, have fused them together and created relatively homogenous batholiths (Bartley et al. 2020). It can be generalized that magmatic arcs, continental and oceanic, demonstrate a great variety of sizes and styles of the magmatic systems (Costa, 2008, Annen, 2009). We thus explore the controls on the diversity of global magmatism in arcs and continental intraplate settings using our 2D modeling. We vary the intruded magma composition (basalt or rhyolite), flux intensity per km^2, and demonstrate that that the magma flux and the distribution of the magma flux are the two parameters that can explain multitudes of these observations.

We are motivated to further investigate questions of crustal melting without prescribing a geometry and displacements to the intrusions. In this sense, we get a detailed view of melting and magma accumulation processes across a growing magma body. A simple kinematic model allows introduction of volcanic eruptions and system response to magma evacuation. We further investigate how the rate, distribution, and composition of magma flux influence the distribution of zircon age populations using a simplified T-X phase diagram and zircon growth-dissolution software of Bindeman & Melnik, 2016 that reads temperature-time-melt fraction properties in each Lagrangian particle.

2 Materials and Methods

2.1 Mathematical model

Figure 1. A) A conceptual framework of the model showing an interconnected network of dikes and sills that cause melting of country rocks (width, height and the third spatial dimension are labeled by W, H and L, respectively). Dike to sill transitions occur above a specified depth in the model. B) Mid-Jurassic Karadag pluton (coastal Crimea) showing similar ellipsoidal dike structure, with columnar jointing marking each individual dike. (photo by A. Tugolesova)

A conceptual framework of the model is presented in Fig. 1. We assume that injection occurs in 2D plain geometry. Each individual dike is approximated by an ellipsoid with semi-axes a and b. We use an analytical solution (Muskhelishvili, 1977) to calculate host rock displacement for a constant Young's modulus, E, and the Poisson's ratio of the host rocks, . Each dike contains either andesitic or rhyolitic magma with a specified temperature, while host rocks are granitic

in composition and are elastic with fixed properties. The initial temperature distribution is linear with a specified geothermal gradient. Injection of individual dikes leads to displacement of elastic host rocks and initiates heat transfer that causes country rock melting and intruded magma solidification. The volume of the individual dike and the frequency of emplacement is controlled by the specified influx rate of the magma to the magmatic center, Q_{in} (km^3/y). The flux is laterally varied in different simulations from defocused to more centrally focused by specification of a normal or uniform probability distribution of the coordinates of the dike centers. In order to calculate the volume of injected magma, the third spatial dimension (horizontal extent of all dikes) is specified at L= 10 km and kept constant throughout the simulations although this length can be different for specific magmatic systems. This situation is possible in the extensional tectonic environment (e.g. Basin and Range province), where the local stress field leads to preferentially parallel dike orientation. We allow a random angle for the individual dike emplacement or the change in the dike orientation from sub-vertical at depth to sub-horizontal near the surface reflecting dike to sill transition (Barnett & Gudmundsson, 2014).

Rock and magma temperature evolution T is governed by the heat conduction equation that accounts for advection due to rock and magma displacement, latent heat of crystallization and heat conduction. Here is the density (indexes "r" and "m" reflect the host rock and magma respectively), C is the heat capacity, is the advective velocity, k is the conductivity, L is the latent heat of crystallization, is the mass fraction of crystals that depends on temperature according to magma type (see Supplementary Fig. S1 for diagrams), is the volume fraction of magma in the rock-magma system introduced as .

The emplacement of a dike is considered instantaneous. Therefore, the velocity field is determined based on the displacement field arising from the loading of an elliptical crack. The values of the semi-axes a and b, as well as the angle of dike injection are set randomly at certain intervals. The number of dikes emplaced during a time step is calculated in such a way that the average increase in magma volume is equal to a given magma influx rate for the area.

We assume elastic rock response in our model to keep the mechanical problem relatively simple and separated from the thermal model in this study. Accounting for viscoelastic properties of rocks and solidifying magma, heterogeneities of rheological properties within the domain, volatile exsolution and transport, local tectonic stresses and other complexities will require the solution of a coupled thermo-mechanical-chemical problem that is extremely difficult for wide ranges of physical properties across the system. The model captures the initial stage of magma chamber formation well when the melt volume fraction is relatively small, but we expect deviations in velocity field calculations as the system matures (melt volume fraction becomes close to 50% when viscous deformation becomes dominant).

As an initial condition, a constant thermal gradient is specified. The temperature at the top and the bottom of the computational domain is kept constant.

On all other boundaries conductive heat flux is set to zero. We place outer boundaries of the domain far from the magma injection area in order to reduce the influence of boundary conditions on the temperature distribution inside the growing magma chamber.

2.2 Numerical method

Discretization of equations (1) is carried out by the control volume method (Patankar, 1980). Modeling thermal evolution of individual dikes with characteristic width of 10-20 m in a domain spanning tens of kilometers requires extremely high resolution of the computational grid. In implicit numerical methods, solving for the discretized system of equations usually involves assembling of sparse matrices and direct or iterative sparse solver. For large-scale problems with tens of millions of degrees of freedom, such an approach is very computationally and memory demanding. During the last decade, a new generation of hardware architecture emerged, originally specialized for computer graphics purposes. Graphics cards, or GPUs, are very efficient for parallel data processing provided that the algorithms are carefully chosen to optimally utilize the hardware.

In this work, we created a numerical code for the Nvidia GPUs in CUDA C language. We use the simplest explicit forward Euler scheme for time integration. In spite of timestep limitations imposed by the stability conditions, the parallel algorithm performs significantly faster than the serial implicit ADI solver, which we attempted in early stages of model development. On a Tesla V100 GPU it takes less than 10 minutes instead of one week of serial CPU computation on the grid of 5000 x 3200 points with spatial resolution of 5 m and total magma injection time of 100 ka.

The volume fraction of the intruded magma is stored in each cell of the computational grid in order to calculate thermophysical parameters of the magma/rock mixture. Injection of a new dike leads to advection of the volume fraction in accordance with the displacement field around the dike. Grid-based methods, such as the method of characteristics, suffer from significant numerical diffusion, which leads to unphysical mixing between magma and surrounding rocks.

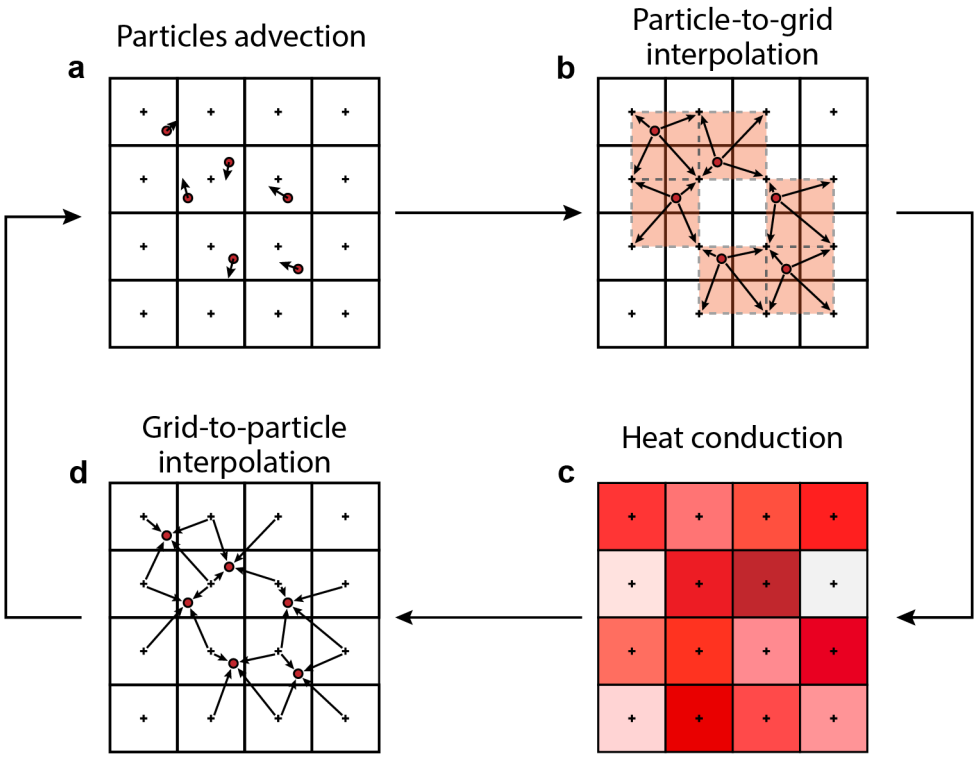

Figure 2. Outline of the PIC/FLIP method used for advection of temperature and volume fraction. The algorithm consists of four stages, repeated at every simulation time step: (a) particles advection, where the Lagrangian particle positions are updated; (b), particle-to-grid interpolation (dike volume fraction and temperature T, are transferred from particles to grid using bilinear interpolation); (c) heat diffusion is solved on the grid; (d) grid-to-particle interpolation (updated values of temperature are transferred from grid back to particles locations using FLIP correction).

To reduce numerical diffusion, the hybrid PIC / FLIP (Particle-In-Cell/Fluid-Implicit Particles) method is used to determine the volume fraction of magma and for advection of the temperature field (Brackbrill and Ruppel, 1986). As shown on Fig. 2, in addition to the grid, the continuous medium is also discretized by a set of marker particles that store a flag indicating whether a particle belongs to the magma or surrounding rocks, as well as the temperature at a point in space corresponding to the coordinates of the particle. For each particle, its displacement can be calculated precisely based on the analytical solution of Muskhelishvili (1977). After that, the volume fraction of magma at grid cell centers is calculated by bilinear interpolation from each particle to the four cells closest to the particle. Thus, the numerical diffusion for the transfer of the volume fraction of magma is significantly reduced.

Since the heat conduction equation is additionally solved for the temperature field on the grid, according to the original PIC method, it is necessary to interpolate the temperature from the grid back to the particles. It can also lead to numerical diffusion of the temperature field. The FLIP modification to the PIC method, developed by Brackbrill and Ruppel (1986), is designed to interpolate not the temperature field itself, but only the difference between the temperature obtained by interpolating from the particles onto the grid and the temperature after solving the heat conduction equation. This significantly reduces numerical diffusion but leads to the unphysical noise in the regions with large temperature gradients (e.g., on the boundary between the dike and rocks). A common solution to this problem is to add a small fraction of PIC interpolation to the result, usually about 5%, which makes it possible to smooth out these oscillations by adding a small amount of scheme diffusion, which is negligible compared to physical heat diffusion due to thermal conductivity. When a new dike is introduced, new particles are generated.

Validation of the numerical code is presented in the Supplementary material (Text S1-S2 and Fig S2-S4). The model presented above allows users to study a wide range of magmatic phenomena. The driver routine is written in MATLAB and allows for the prescription of 1) physical properties of the rock and magma, 2) the depth, distribution, angles, and sizes of injected dikes, 3) the proportion of dikes to sills, the dike to sill transition, and the distribution vs depth of intrusions, and 4) magma emplacement intervals with different influx rates and durations for each injection episodes. It creates binary files that store all parameters for the GPU simulation. All results are stored in the HDF5 file format, which can also be visualized in MATLAB. The program and algorithm are accessible to anyone with minimal programming skills and is designed to be modified by the users to conform to specific geochemical and geophysical constraints for any magmatic or caldera system of interest.

3. Results

The examples and parameter values presented below model magma genesis in a typical magmatic arc setting and demonstrate the capacity of the model to mimic basic scenarios for the formation of magma chamber by rhyolitic and basaltic magma intrusions. Parameters that are used in simulations are listed in Table 1.

We study formation of a magmatic system in the upper crust (first 15 km) and fix the horizontal dimension parallel to the dike orientation to 10 km. Most of simulations were performed for the width of the magma injection region of 10 km. That results in the area of the magmatic center of 100 km^2. With these settings we specify volumetric magma flux in m^3/s (1 m^3/s 0.03 km^3/a which is equivalent to $3x10^{-5}$ $km^3/a/km^2$).

The choice of magma intrusion rates is of course the leading parameter in determining the magma output and zircon survival, so we place our assumptions in the framework of published research. Schöpa and Annen (2013) suggest tran-

sient high fluxes of at least 1.25 × 10^{-2} km^3/a to generate magma chambers with volumes of 500-2000 km^3. Caricchi et al (2016) explored the range of magma flux of 10^{-4}–10^{-1} km^3/a, Gelman et al. (2013) studied magma injection into a cylindrical domain with the radius of 10 km and magma fluxes of 0.005-0.03 km^3/a. Other authors (Tierney et al., 2016, Rummel et al., 2020, Karakas et al., 2017) suggest magma fluxes of 0.1-6 x10^{-3} km^3/a. A global compilation of 170 time-averaged volumetric volcanic output rates was collected in White et al. (2006). They found that more silicic compositions (2.3 ± 0.8 × 10^{-3} km^3/a for andesites, 4.0 ± 1.4 × 10^{-3} km^3/a for rhyolites) have a more limited range of eruption rates than basaltic eruptions (2.6 ± 1.0 × 10^{-2} km^3/a). All of the volcanoes on continental crust have an overall average of 4.4 ± 0.8 × 10^{-3} km^3/a. White et al. (2006) suggest a plutonic to erupted ratio of 5:1 as a common value leading to ~ 2.2 × 10^{-2} km^3/a magma intrusion rates. In our study we vary the rates of magma supply in a range of 0.125-1 m^3/s equivalent to 0.4- 3 × 10^{-2} km^3/a.

3.1. Rhyolitic dike injection into granitic crust

We first present simulation results for liquidus magma (0% crystals, T=950 °C) of rhyolitic composition injected sequentially as dikes and sills into the crust of the same, fully crystalline granitic composition. Depths of injections vary between 4 and 13 km, typical depths of crustal magma chambers and batholiths, with an initial temperature gradient of 40 °C per km from 200 °C at the top of the injection interval to 560 °C at the bottom. The total depth range of computational domain is 16 km and the total width is 26 km. This setup simulates formation of upper crustal plutons and magma bodies containing eruptible magmas.

Parameter	**Description**	**Value**
	Density	kg/m^3
$_{\mathrm{r}}$	Thermal conductivity of rock	W/m/K
$_{\mathrm{m}}$	Thermal conductivity of magma	W/m/K
C_p	Specific heat capacity	J/K/kg
L	Latent heat of melting	×10^5 J/K/kg
T_{m}	Magma intrusion temperature	Basalt: 1170 C Rhyolite: 950 °C
T_{top}	Temperature at depth z = 5km	°C
T	Temperature geothermal gradient Possion's ratio of rock	°C/km
E	Young's modulus of rock	GPa
Q_{in}	Intrusion rate	– 1 m^3/s

Parameter	Description	Value
$z_{\min}$,$z_{\max}$]	Dike center depth	– 14 km
W	Width of dike intrusion region	– 15 km
$zs_{\min}$, $zs_{\max}$]	Depth range of sills formation	– 8 km
	Dike rotation angle	° – 95°
a	Dike half length	– 1500 m
b	Dike half thickness	– 20 m
h	Dike transverse width	km

Table 1. Parameters used in the simulations.

Fig. 3 presents the graphical results of calculations of the melt fraction evolution during formation of a magma chamber at different stages of its growth and cooling. Regions with a melt fraction greater than 0.5 are contoured as it corresponds to the average rheological extractability window (Marsh, 1981) and thus contain potentially eruptible magma. Magma injection rates of Q = 0.125, 0.25 and 0.5 m^3/s (0.004-0.03 km^3/year) and the widths W of the injection region ranging from 5 to 15 km, resulting in the flux intensity of 7.9, 7.9 and 10.5 $\times$ 10^{-5} km^3/a/km^2, respectively. Dikes are introduced sub-vertical in the range of depths from 13 to 4 km. The injection zone grows in vertical and horizontal as the system swells by vertical and lateral extension. Given that dike intrusions are changing orientation to sills as is abundantly seen in nature (Fig. 1b, McBirney, 2006; Thomson, 2007) and experiments (Menand et al. 2010), we adopt such transition in the model. We assume that if the center of the dike is at a depth below 5 km, then the emplacement of the magma becomes sub-horizontal (sills). Such a situation is common in the areas of active volcanism and may be associated with the distribution of the density of the host rocks (level of neutral buoyancy for the magma, (Walker, 1989) or the presence of layers with a larger Young's modulus (Barnett & Gudmundsson, 2014), e.g erupted volcanic or sedimentary rocks. The analytical solution that is used to calculate the displacements of host rocks in the current model cannot be applied for the latter case as it assumes homogeneous elastic rock properties.

In the first set of simulations, injection occurs during the first 100,000 years (100 ka) and involves dikes of either rhyolitic or basaltic composition emplaced into granitic crust. We use the Piwinskii (1969) phase diagram (see supplementary Fig. S1 for temperature-melt fraction relationships) to account for melt fraction. No volcanic eruptions (removal of melt and heat) are allowed, thus, these simulations correspond to maximum possible melt production and accumulation, which approximate shallow pluton formation. We track the percentage and the distribution of areas with >50% (eruptible magma), and >1% melt (solidus), and the resulting amount of the crustal melt vs intruded melt throughout the intrusion.

In all three cases, a large body of eruptible magma (melt >50%) is formed after 100 ka. The first two cases are similar in behavior because they correspond to the same flux intensity (flux per unit area). After 75 ka small unconnected batches of eruptible magma are formed in a large volume of crystal mush with 25-40 vol% of the melt mostly at the bottom of the injection region where the temperature is higher. At later stages, dike injection leads to the formation of a large volume of eruptible magma containing both molten crust and the newly injected material. Similarity in these two cases means that the process is dominated by the advection of a temperature field and latent heat release/consumption rather than conductive heat transfer.

For $Q = 0.5$ m^3/s, the flux intensity is larger and two areas of eruptible magma are formed after 75 ka of rhyolitic dikes intrusion. The upper domain corresponds to dike-to-sill transition depth where the heat release is higher due to geometric arrangements. The two domains become completely merged after 100 ka with a formation of a magma reservoir with a volume of more than 1000 km^3, theoretically capable of producing caldera-forming super eruptions The total amount of injected magma is 1577 km^3 for this case corresponding to 1:1.6 high efficiency magma production. On the contrary, the case with low flux intensity ($Q = 0.125$ m^3/s, W =10 km, Fig. 4, 25-90 ka) produces virtually no eruptible magma during 100 ka of intrusion resulting in a magma production efficiency of zero.

3.2. Simulation of magmatic unrest

Efficiency of melt production and formation of molten magma bodies strongly depends on the magma influx rate into the upper crust. Fig. 4 presents snapshots of melt volume fraction for an eight-fold change in the magma influx rates Q from 0.125 m^3/s for 90 ka to 1 m^3/s happening during the last 10 ka. At these flux rates, 3548 km^{3}of injected magma produced a crystal mush body (consisting mostly of solidified intruded material) with low melt fraction. Injection of similar amount of magma (3154 km^3) during last 10 ka results in the formation of distributed, vertically-elongated pockets of low crystallinity melts that are capable of merging and erupting.

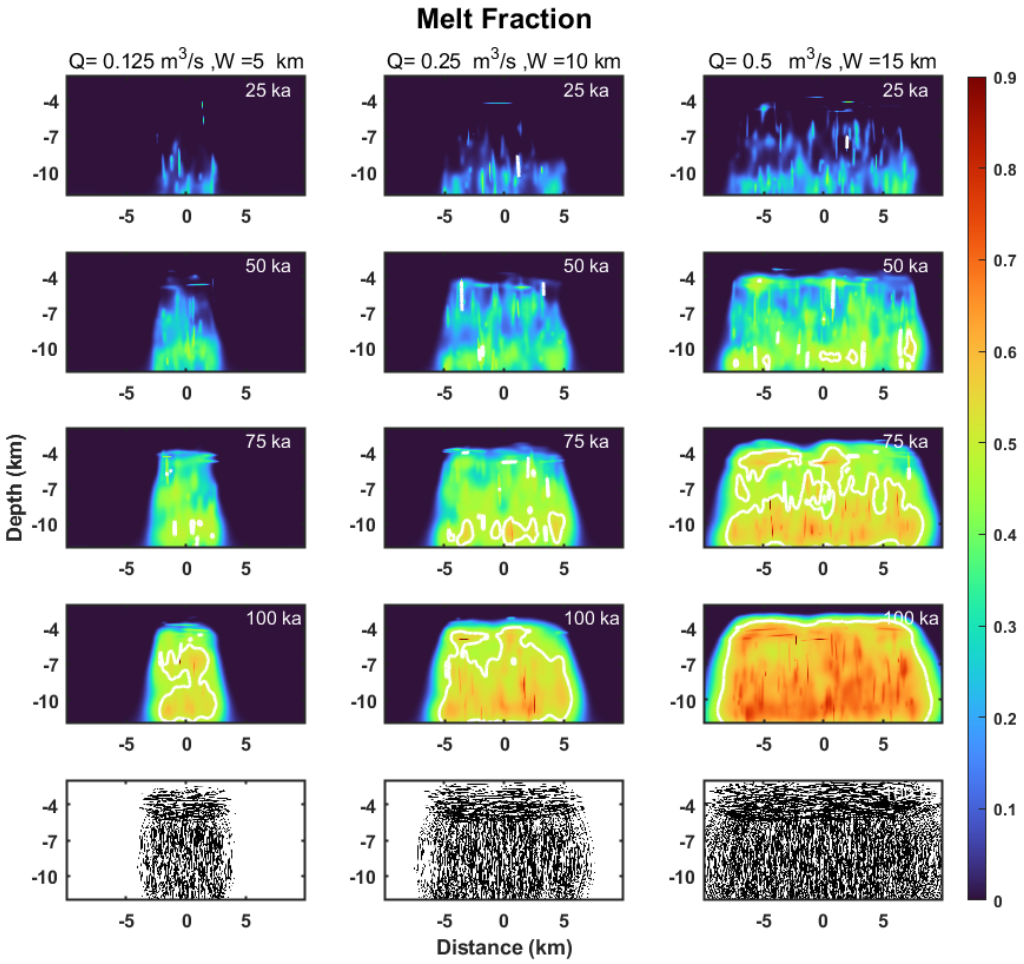

Figure 3. Stages of growth of the magma body for 100 ka at different magma flux rates Q by injection of dikes and sills without eruptions. Evolution of melt fraction in the magma body grown due to sill and dike injection for indicated amount of time. Each vertical column represents a separate case with a different rate Q, and injection zone W. White contours show regions with eruptible magma (melt fraction $>$ 50 vol%). Last panels show all injected dikes/sills at the end of the magma body growth.

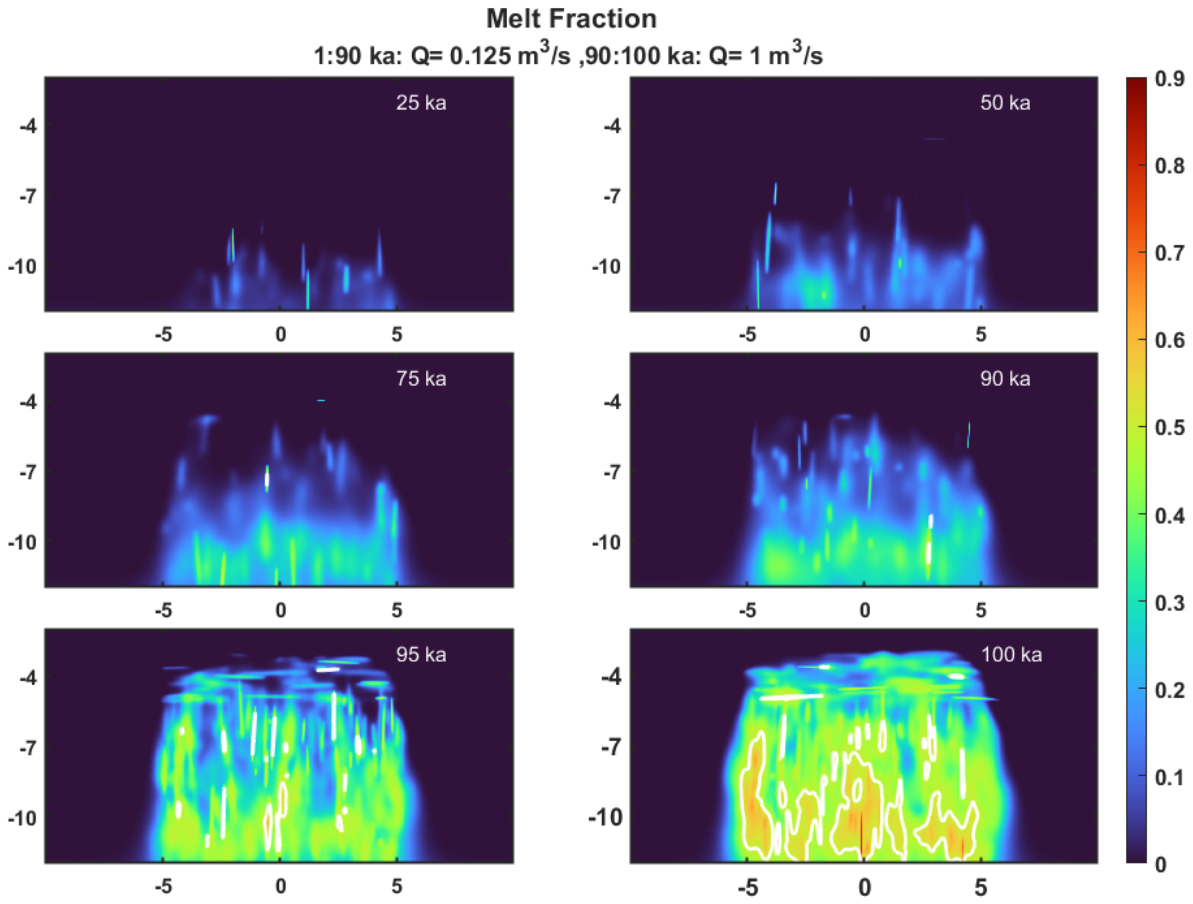

Figure 4. Simulation of the magmatic unrest. Magma influx rate increases by 8 times during last 10 ka leading to the formation of interconnected melt pockets with variable proportion of intruded magma an molten country rocks.

3.3. Basaltic dike injection into granitic crust

The second set of models included basaltic dike intrusion into granitic crust. Basalts have higher solidus and liquidus (see supplementary Fig. S1) temperatures and according to the adopted phase diagram can differentiate to more silicic magma at lower T (Fig. S1). Fig. 5 shows simulation results for liquidus basaltic magma injection to granitic crust at temperature of 1170 °C and melt fraction vs. temperature dependence taken from Nandedkar et al. (2014).

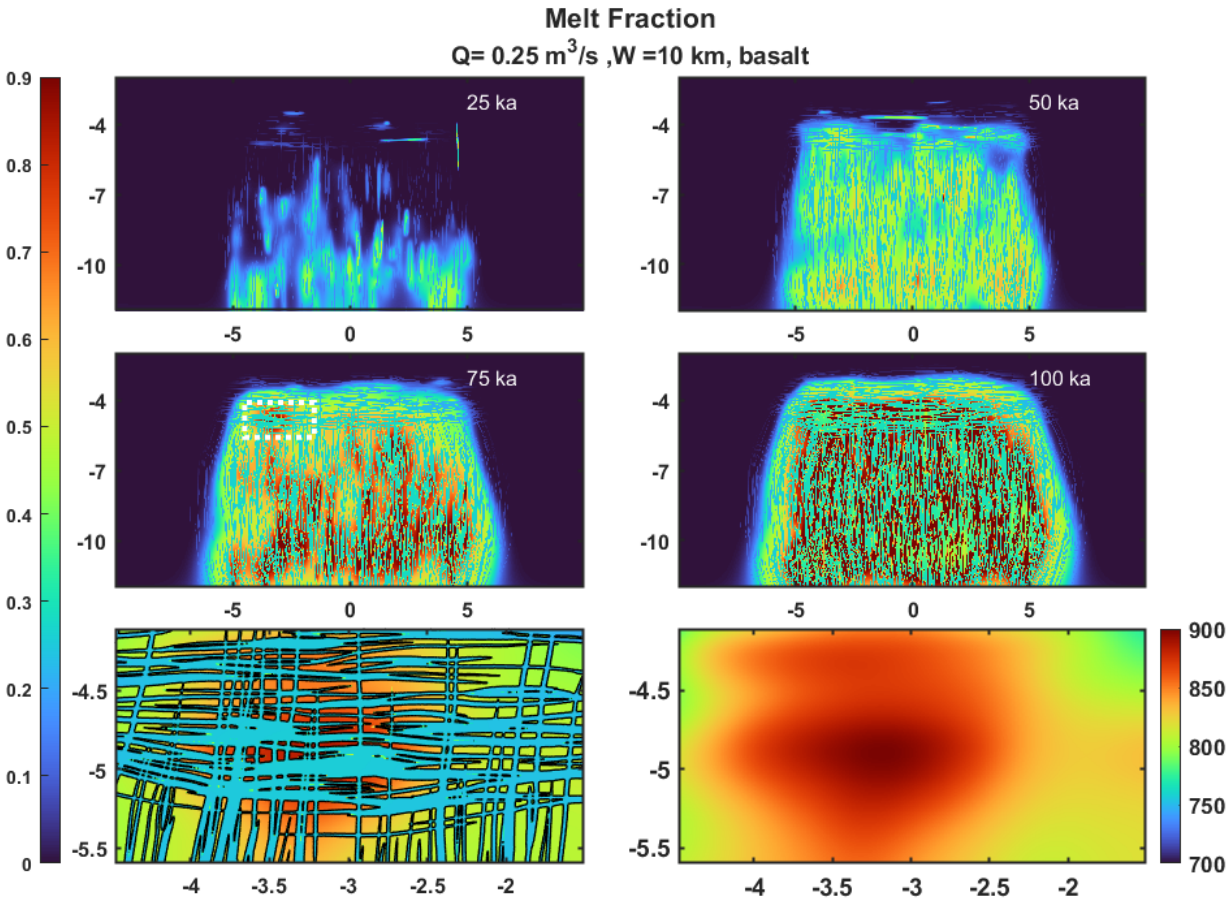

Figure 5. Distributions of the melt fraction in the case of injection of the hotter basaltic magma into granitic crustal rocks with a constant Q = 0.25 m^3/s for 100ka. The magnifier shows detailed melt fraction and temperature distributions in the region shown by dashed rectangle for the time of 75 ka. Compare with Fig 3 for rhyolite to granite injection.

Basaltic magma solidifies at higher temperatures releasing the latent heat of crystallization and providing heat to granitic rocks with lower melting temperature. As a result of heat exchange, a patchy structure of highly crystalline basalts in strongly molten rhyolite emerges. Such structure will prevent magma mixing because dikes form a high viscosity carapace (see left bottom panel). Intrusion of basaltic dikes generates rhyolitic partial melt in the country rocks and a residual melt of variable SiO_2 within interstitial spaces between basaltic intrusions. At large melt fraction, melts would segregate and higher temperature restites would sink, but this is not currently taken into account.

3.4. Kinematics of magma chamber formation

Fig. 6 shows the kinematics of Lagrangian particles associated with rocks and magma for the case of Q = 0.25 m^3/s (Fig. 3, central column). In the dike injection region, displacement is preferentially horizontal and downward, while intrusion of the sills leads to a vertical displacement (uplift) of several hundred meters over 100 ka without taking account of surface erosion or dynamics. Particles near the central line of the intrusion exhibit a small horizontal shift, dikes injected at later stages largely stay within the injection region, while the early injected material is pushed to the periphery of the intrusion, in a fashion similar to spreading. The maximum displacement during the active diking period of 100 ka exceeds 5 km at depth and a 1-2 km near the surface, while thermal equilibration length-scale on this timescale is on the order of 1 km. It means that during the formation of the magma chamber heat transfer is dominated by advection and latent heat release/consumption at the periphery of magma chamber while conductive heat transfer is dominant in the central part of the intrusion zone where displacements are smaller. This is a novel result of our 2D simulation with elastic displacement of rocks, not seen in previous models.

Surface uplift in the middle of the domain reaches 700 m, resulting in the mean uplift rate of 0.7 cm/year. The uplift remains large even at a distance that is 6 times larger than the initial magma emplacement region or 3 time larger than the region occupied by the magma at the end of the emplacement period. Maximum horizontal displacement is comparable with vertical and corresponds to the distance reached by the dikes.

For the case shown on Fig. 4 the uplift is only 0.2 cm/year during the magmatic build-up stage and it increased up to 2 cm/year during the unrest period. These uplift rates are comparable with those measured on active volcanoes (Newhall and Dzurisin, 1989; Lowenstern et al. 2006), the fastest of which is 20 cm/year under Laguna del Maule (Zhan et al. 2019).

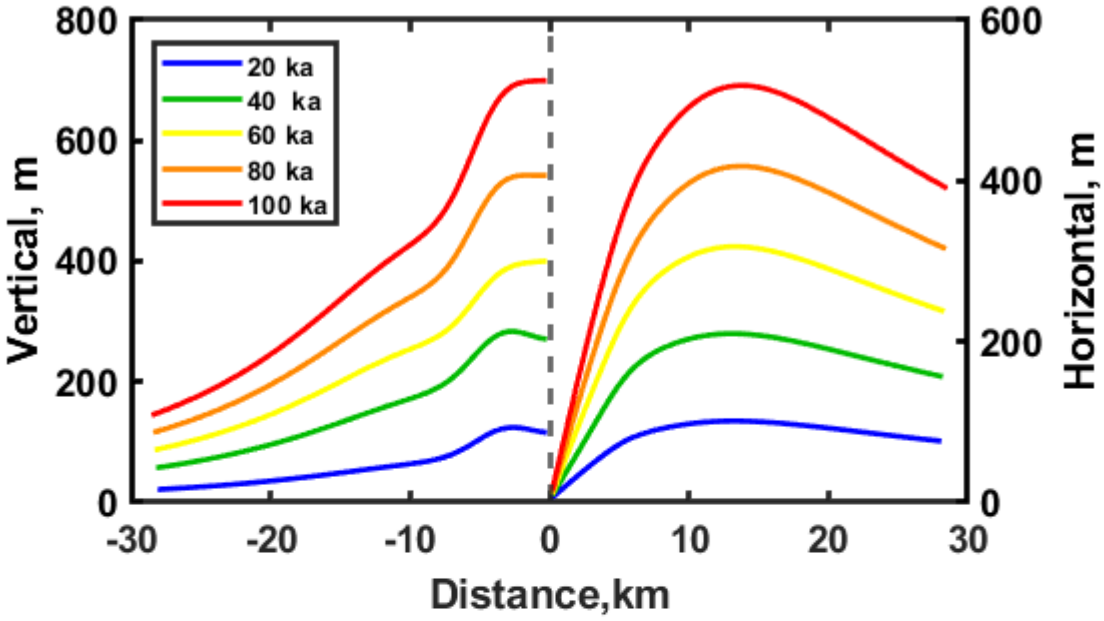
800
600
400
200
0
Vertical, m
600
400
200
0
Horizontal, m
20 ka
40 ka
60 ka
80 ka
100 ka
-30
-20
-10
0
10
20
30
Distance,km

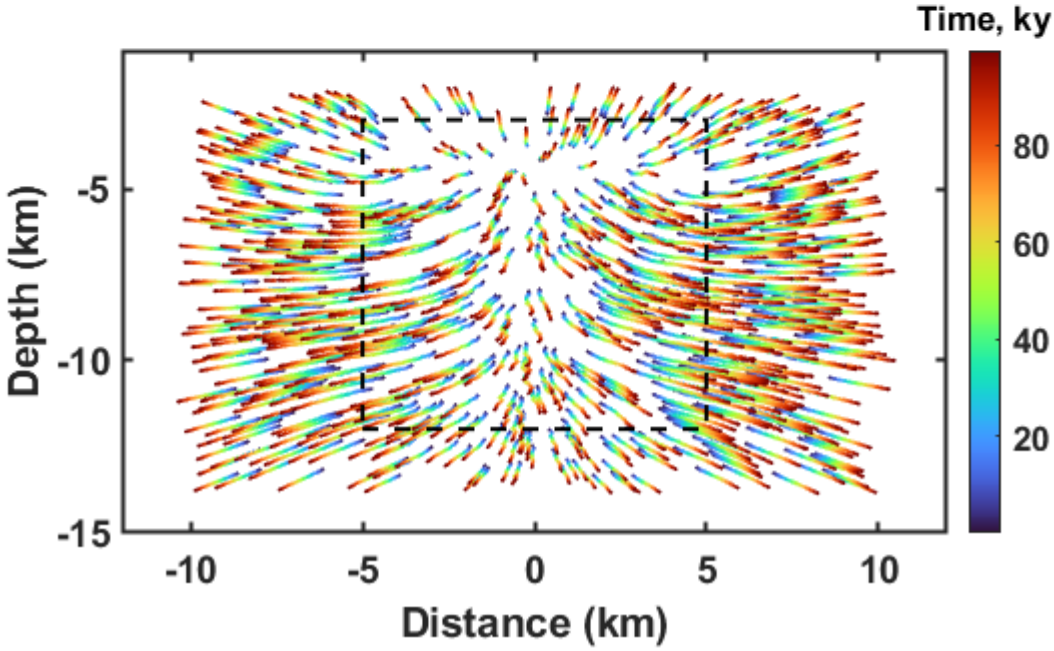
Time, ky
80
60
40
20
Depth (km)
-5
-10
-15
-10
-5
0
5
10
Distance (km)

Figure 6. Vertical uplift, horizontal surface displacement, and trajectories of individual Lagrangian particles during 100 ka of dike and sill injection. Particle color represent time since the beginning of the model (magma influx). Injection region is shown by dashed-lined rectangle, notice horizontal and vertical spreading away from this region.

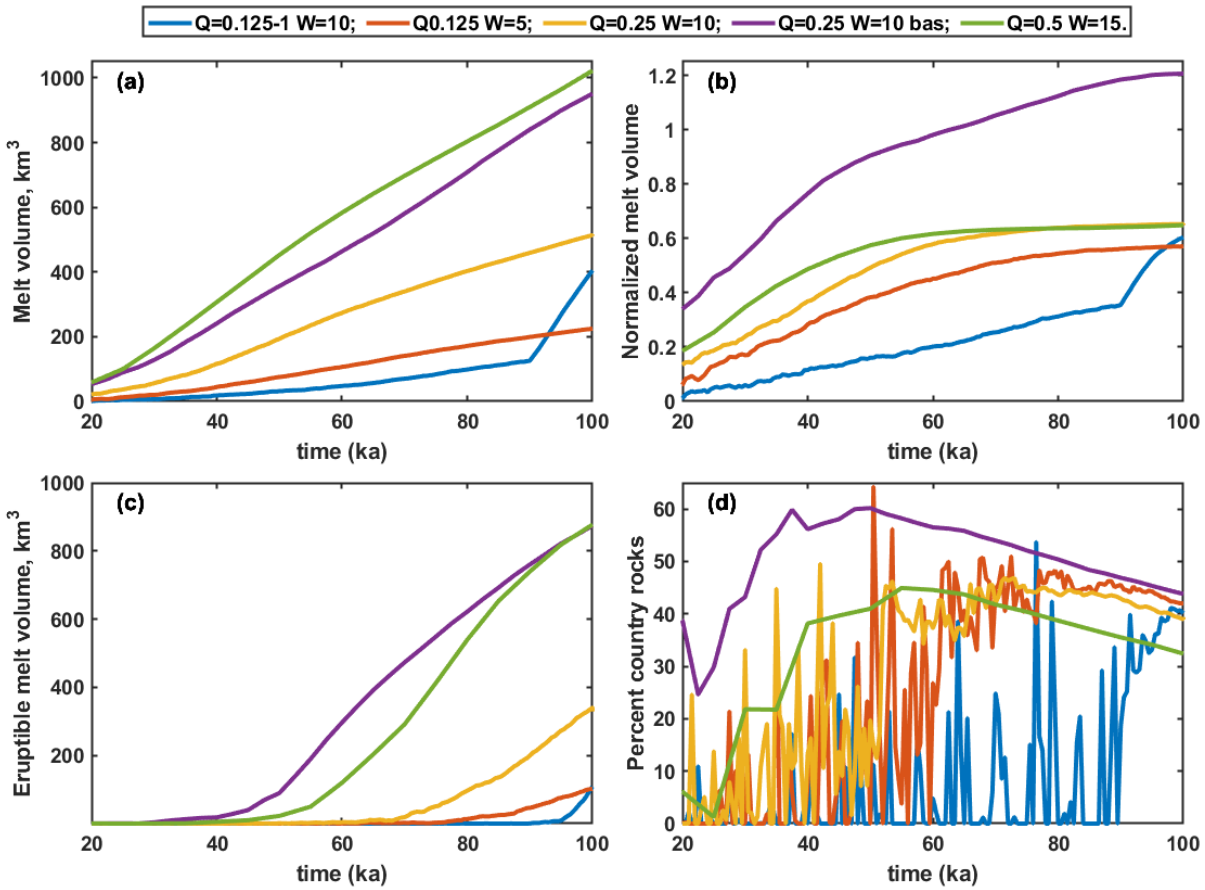

Figure 7. Melt volume for different injection rates and width of the domain (a) – total melt volume, (b) – total volume normalized by the volume of injected magma, (c) eruptible (melt fraction > 50 vol%) magma volume, and (d) percentage of country rocks in eruptible magma. Strong oscillations correspond to small volumes of eruptible magma batches with highly variable composition.

3.5. Melt production rates and host rock assimilation

The amount of country rock melt that may be generated by rhyolitic and basaltic dikes (melting efficiency) and the total amount of eruptible melt are important parameters to consider. Fig.7 explores the extent of crustal melting induced by the rhyolitic and basaltic magma intrusion by specifically tracking the regions

with country rock melting (>1%), and for eruptible magma (in which total melt fraction exceeds 50%). This number is taken as a simple measure or rheological extractability of magma from mushy zones (e.g. Marsh, 1981; Huber and Parmigiani, 2018). We explore different magmatic intrusion cases presented above on Fig. 3-5, resulting in dramatically different total magma production. For Q = 0.125 m^3/s and W = 10 km, there is no significant eruptible melt formed during the first 90 ka of the dike intrusion. Only when Q increases to 1 m^3/s does an eruptible melt volume form resulting in a 350 km^3 crystal mush body after 10 ka of the unrest. For W = 5 km the same eruptible volume forms at the end as a result of magma injection at constant rate during 100 ka. The highest melt production rate corresponds to the largest among simulated magma influx rate (Q = 0.5 m^3/s). Injection of hotter basaltic magma with twice this smaller rate (Q = 0.25 m^3/s) results in a similar total melt volume in the same conditions. For the case of basaltic dikes, production of eruptible magma starts earlier mainly due to significant melting of the host rocks. Melt production normalized to the mass of injected magma trends towards a constant value of ~ 0.6 for rhyolitic magma intrusion and goes above one for basaltic. Therefore, as the system matures the efficiency of the melt production becomes buffered by the heat conduction and the increase in the volume of the system (Fig. 7b). Basaltic magma injections into an already thermally matured system result in a net production of melt.

A special melting case, called crustal cannibalization (Bindeman and Simakin, 2014), occurs when either rhyolitic or basaltic dikes intrude buried tuffs and lavas with large amount of glass, especially in intracaldera systems. In such cases, initial dike intrusion will cause effective melting without latent heat consumption during devitrification of glass. Energy balance modeling suggests this scenario is comparable to 100-150°C higher effective ambient temperature of country rocks, causing ~25% more efficient assimilation (Simakin and Bindeman, 2012).

The percentage of partially-molten rocks in the eruptible magma also increases with time (Fig. 7d) before reaching a maximum value, and then starts to decrease because a significant amount of the host rocks are shifted towards the periphery of the growing magma chamber where they cool and solidify. Due to their higher temperatures, basaltic magma assimilate host rocks more efficiently in comparison with rhyolitic (up to 60 % at maximum vs. 45-50 %).

3.6. Simulation of eruptive activity

Simulations described above assumed that all injected magma stayed inside the host rocks causing their uplift and spreading, and formed a plutonic magma body largely consisting of mush with isolated melt pockets. Next, we present result of modeling permitting melt removal by eruption from these melt zones and its effects on overall thermal and compositional evolution of the system. This is achieved by reversing spreading into contraction in our elastic model. As our model is not capable of calculating global thermomechanical stress field changes due to dike emplacement and magma chamber growth, thus, cannot predict the trigger point for the onset of eruptive activity, which is generally

a complex topic to model dependent on many parameters. Instead, we here use kinematic approach to simulate removal of magma by eruptions from the growing reservoir by using log-linear magmatic volume -frequency relationship observed in nature (Papale, 2018). We first randomly generate a set of possible volumes Ω_i of individual eruptions ranging from 1 to 1000 km^3 (VEI 5-8) and here specify a typical volcanic to plutonic ratio = 0.2 (1:5, e.g. White et al., 2006). We then track individual interconnected eruptible melt batches naturally generated in our model, and compare their volumes with $\Omega_i/$. If the volume of the batch exceeds the volume of current eruption, we remove it by the algorithm described below during 1 time step. The next eruption starts similarly when the next batch accumulates a critical volume. This approach allows to produce different sizes of eruption distributed by a specified volume-frequency law. For particular volcano-magmatic system this law can be tuned based on historical reconstruction of the eruptive history, and volcanic to plutonic ratio can be adjusted based on available geological, geochronological, and geophysical information. The shape of the interconnected magma batch can be rather complicated as is seen in our models (Fig. 9); therefore, we treat each elementary volume of the eruptible batch as a point sink of magma with a specified volume reduction. Displacement from the single volume in each grid cell can be calculated as:

$$U_{\mathrm{XY}} = h^2 \gamma \frac{\vec{r}}{|r|^2}$$

Here h is the grid step size, $\vec{r}$ is the radius vector between the point sink with coordinates [X, Y] and a cell with the center [x, y]. In order to calculate the total displacement of the particle in the cell we make a summation of individual displacements that advect the temperature field accordingly.

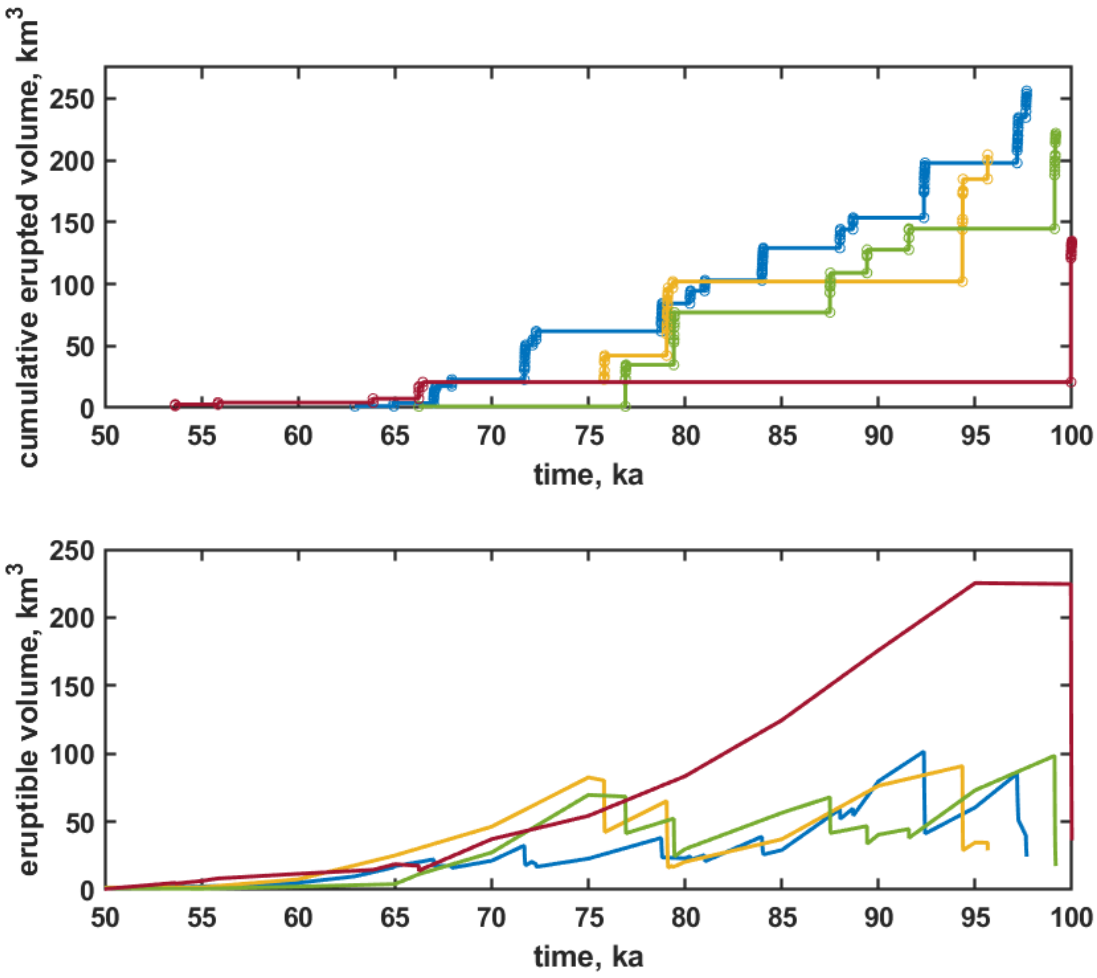

Figure 8. Cumulative erupted volume and the volume of eruptible magma vs. time for Q = 0.25 m^3/s and W = 10 km and different sampling series of eruptive volumes Ω_i. Larger eruptions are preceded by a longer repose time end followed by a sequence of smaller events. The system shown with brown line has only one large eruption at the end.

Fig. 8 shows cumulative erupted volume and the available volume of eruptible magma vs. time for Q = 0.25 m^3/s and W = 10 km and different sampling series of eruptive volumes Ω_i. As an artefact of our approach, eruptions group in sequences starting from a large eruption. The system waits for the accumulation of sufficient volume and erupts it only partially (only Ω_i). If the next eruption has a smaller volume Ω_{i+1}, than the amount of eruptible magma is reduced by Ω_{i+1}. The process repeats itself until the volume of the eruptible magma batch becomes smaller than the volume of the next eruption. After each eruptive

sequence, the volume of eruptible magma starts to recover due to influx of the new magma from below. The total volume of injected magma is equal to 788 km^3. At the end of the active diking period ~ 50 km^3 of magma remain available for consequent eruptions and 250 km^3 was erupted in more than one hundred of events.

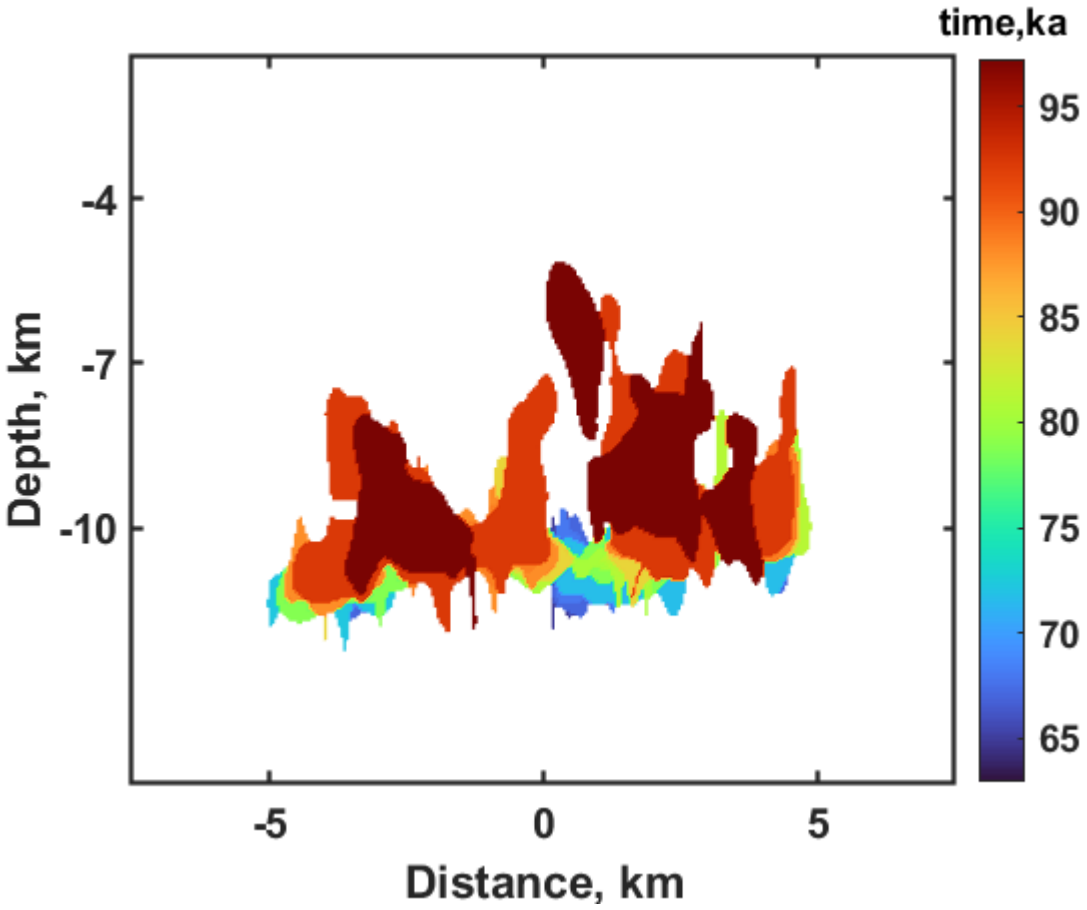

Fig. 9. Locations of erupted batches for different eruptions shown on Fig 8 and color coded accordingly. Several eruptions occur from the same magmatic center, thus, contours overlap. See text for discussion.

Fig. 9 shows locations of erupted batches for different eruptions described in Fig 8. It is noticeable feature of our model that the eruptions start at the lower boundary of the magma emplacement region where temperatures are initially higher and thus melt production is easier. With time as the system matures the depth of the eruptible melt accumulation in the magma system decreases. Most of formed magma batches experience several eruptions in a closely spaced in time sequence until the melt volume decreases below the eruptible volume,

then the activity migrates to a different center.

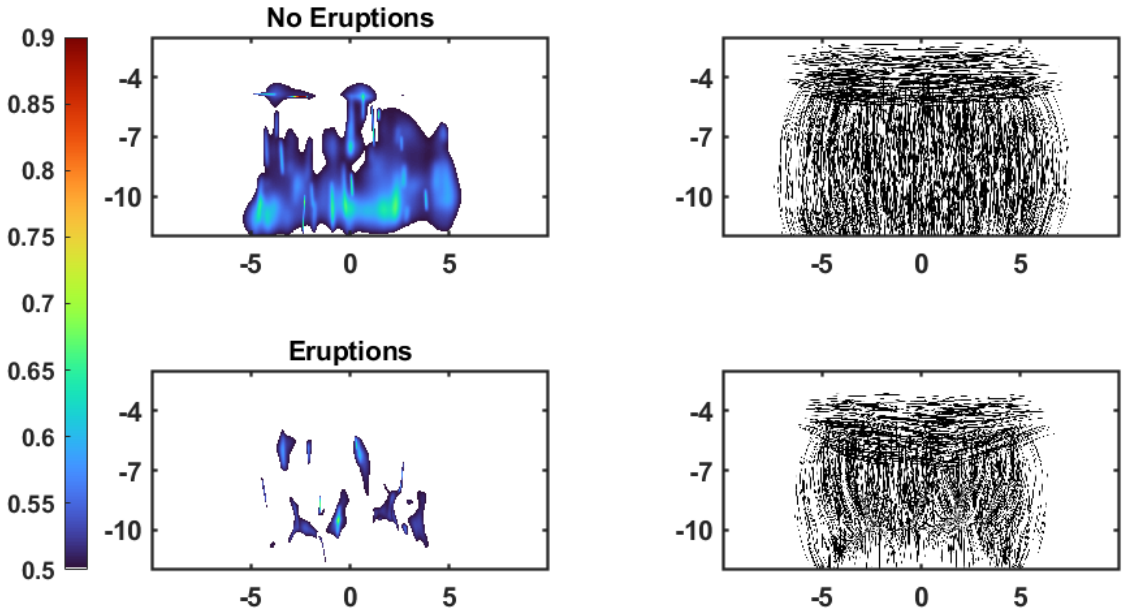

Figure 10. Distribution of the final eruptible melt volume fraction and dike locations with and without eruption after 100 ka of magmatic system development. Notice smaller volume of the systems with eruptions and that the sills on the top of the system are turned inward. Additionally, systems with eruptions are represented by isolated unerupted melt pockets distributed within the crystal mush and solidified portions.

Fig. 10 shows distribution of the final eruptible (>50%) melt volume fraction and dike locations for magmatic systems with and without eruptions as well as the sizes of the magma systems with melt >1%. The volume of total eruptible melt that is possible to get generated over the entire 100 ka duration of magmatism is significantly smaller for system with eruptions. Thermomechanical modeling of Colón et al (2019) observed similar relationships for larger and longer-lived systems using a cruder computational mesh. This is explained by the loss of heat with eruptions. Additionally, horizontal spreading of the magmatic system is significantly reduced and there is a downwards sagging sill displacement associated with predominant evacuation of magma in eruption rooted from central hot interiors of the growing magma body. After 100kyr, sills are inclined towards the center of magma injection region and the top of the magmatic system is displaced down by more than 1 km from the original level. Of course, erupted magma will accumulate on the surface in the form of the cone (not shown) form a layer of deposits that must be accounted in order

to reconstruct the total elevation of the surface (overburden is not considered in this model).

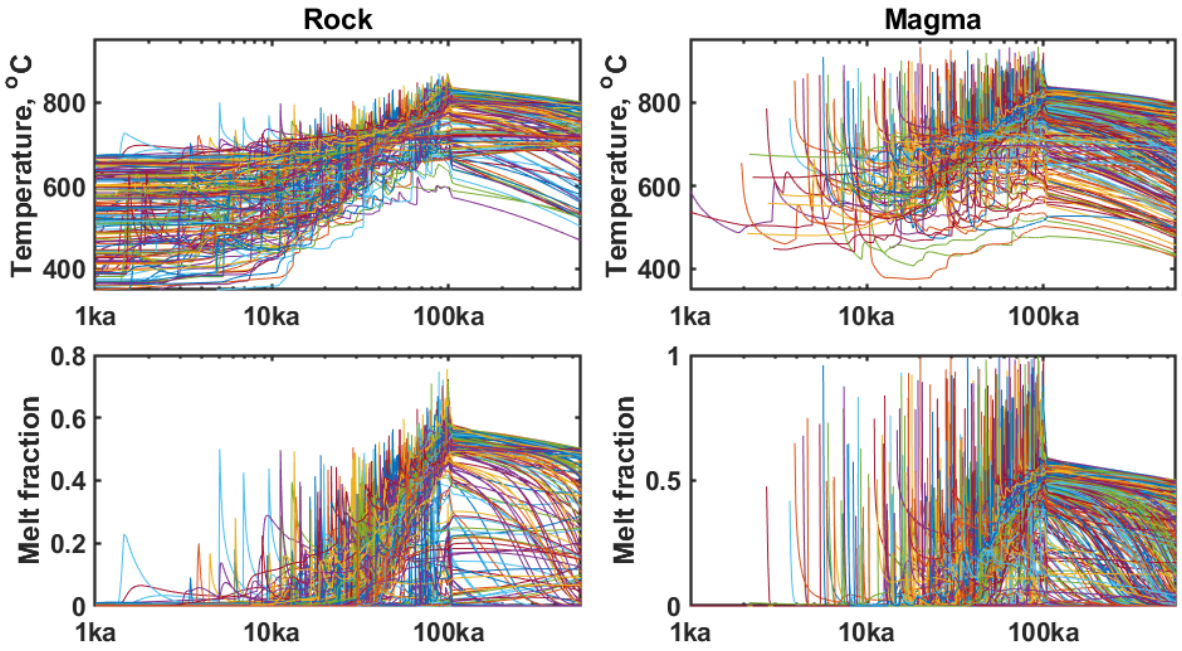

Figure 11. Temperature and melt fraction variation in granitic rocks and rhyolitic magma parcels with time for Q = 0.25 m^3/s and W=10 km, no eruption. Only parcels that reach at least 700 °C are shown.

3.7. Magma and host rock thermal histories

The 2D model presented in this work not only allows investigation of the cumulative thermal and melt fraction evolution of the whole system as was done in the previously published models but permits investigation of the behavior experienced by multiple areas within the growing magma body and country rocks, as well as inside of each dike or a sill (Fig. 1). Country rocks, and previously intruded and now solidified dikes, can experience a non-trivial, spatially- and temporally independent series of heating, melting and crystallization episodes. Thus, the model presents a more realistic scenario for natural situations, and these changes will be reflected in their crystals including zircons. Furthermore, consideration of elastic displacement of rocks after intrusion in our model (spreading), provides an additional, previously underexplored feedback between mass and heat advection, melting and crystallization in different parts of the system.

Fig. 11 shows the dependences of the melt fraction and temperature on time for Lagrangian particles associated with magma and host rocks for injection of rhyolitic dikes in granitic crust for $Q = 0.25$ m^3/s and $W = 10$ km. Each

early injected magma portion cools down quickly and completely solidifies during first 1-2 ka, but later intruded magma and country rock stays molten for a long time, until the temperature of the whole magma body drops down below the solidus. Rocks are not significantly melted by the magma at the first stage of the injection (incubation period), but the degree of melting reaches more than 60-70% at later stages of continuous injection and magma chamber formation. Variation of temperature and degree of melting in an individual particle is non-monotonic and experience several heating and cooling episodes depending on its location within the area of dike injection. For example, early dikes cool down quickly and are later displaced to the periphery of the forming magma chamber. At the same time, dikes in the center remain hot and are later remelted and their melt is then reincorporated into the large body of the magma chamber. With progressive dike addition, subsequent dikes deliver heat and mass to a maturing reservoir those temperature increases smoothly. Upon cessation of new magma addition, its temperature decreases monotonically with time. The Temperature- and Melt fraction (X)-time history that we observe in our 2D model confirm "spike, then exponential decay" schemes often assumed in modeling and petrologic literature dealing with magma intrusions (Caricchi et al., 2019; Szymanowski et al., 2017); these are used for example to interpret crystals with complex zoning by solution-reprecipitation. However, T-t and X-t of the present work are different in several important aspects both spatially and temporally. Initial stage of magma chamber growth is characterized my highly inhomogeneous temperature distribution. As magma chamber matures, newly injected dikes do not change its thermal state significantly because the volume of individual intrusion is much less than the volume of accumulated melt.

A comparable temperature history for basaltic magma injection into granitic crust are presented and discussed in Supplementary material, Fig. S4. In comparison with Fig. 11, many of rock parcels become completely molten and stay molten for a long time. None of magma parcels stay completely molten after injection. This is very different from prescribed fixed position injection of the magma simulated in previous models where newly injected magma is always separated from host rocks by previous injections.

Overall temperature and melt fraction evolution in our 2D model inform us on new developments as a result of accounting for whole system spreading at rates faster than heat conduction. In some central parts, the system exhibits behavior consistent with "overplating" models in which newly injected melt is placed on top of the previous magma/rock boundary. This maintains high heat influx rate and causes rapid temperature rise and melting, most other parts of the model considered in this work exhibit less melting that occurs even in the random dikes and sills models of Dufek and Bergantz (2005) or Annen et al. (2006). However overall, T-Xmelt-time trajectories of the different parts of the modeled magma system experience extreme diversity, that span all melting efficiencies from prescribed overplating, to random dike regimes, and thus reflect processes in the real growing magma system.

Calculated Temperature-Xmelt-time trajectories can be used in modeling of crystal destinies. For example, zircon (and other mineral) zoning patterns, can be modeled and interpreted more realistically than previously prescribed spike-decay schemes. Such diversity of regimes can be used to interpret zircon records with diverse ages, that we consider next.

3.8. Zircon evolution

Investigation of plutonic and volcanic systems aims at their formation and evolution is provided by their crystal record, among those zircons is playing increasingly important role. The emerging science of zircon petrochronology (e.g. Schaltegger et al. 2019) where not only domains within zircons can be dated with ever improving U-Th-Pb precision informing on the duration of zircon growth and inheritance, but also the trace elemental zoning pattern within the same spots can provide information on T-Xmelt-time changes (Claiborne et al. 2010; 2018; Melnik and Bindeman, 2018).

This paper adds to these tasks by examining zircon behavior in the course of magma body construction and cooling. For this purpose, we use numerically-generated temperature and compositional history recorded in each marker points (10,000 total markers, related to the spatio-temporal evolution in host rocks and magma) and integrate these with zircon crystallization-dissolution software of Bindeman & Melnik (2016). This relatively straightforward coupling enables reconstruction of dissolution and growth histories of great multitude of individual zircons of the entire system. For example, depending on the time, composition, and the position of the injected magma zircons in it can 1) crystallize rapidly (years-decades) during complete solidification of magma short after its emplacement or 2) crystallize over a prolonged period of time if magma is injected into the hot interior and thus remains molten in a long time and cools slowly with the whole system, 3) crystallize from a dike or a country rock melt, or 4) first crystallize then dissolve multiple times. Zircons in the country rocks can undergo variable amounts of partial dissolution depending on the temperature-time history of each particular marker and preserve or not preserve the inherited core. Similar modeling can be implemented for any other accessory mineral for which there is diffusion and saturation conditions, or a major mineral for which the phase diagram relations can be specified. For example, Bindeman and Melnik (2016) present such algorithms for monazite and apatite.

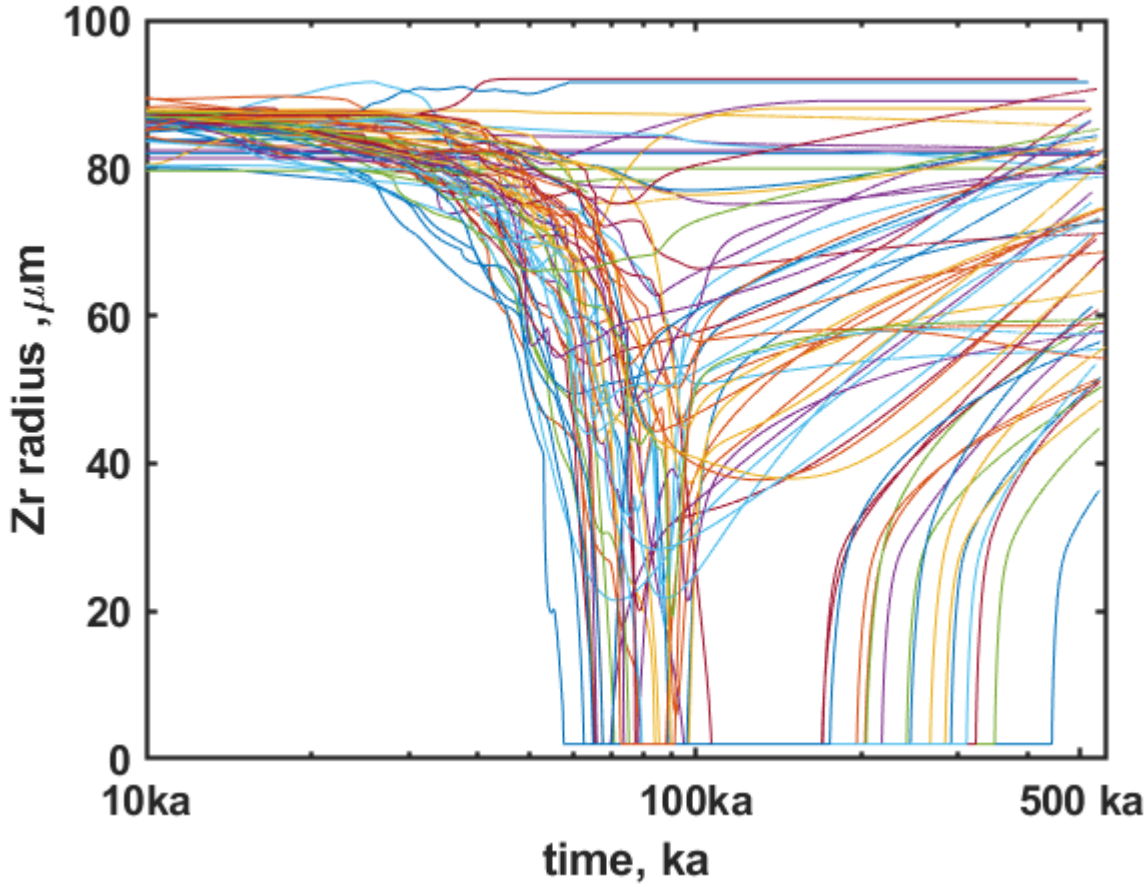

Figure. 12. Evolution of 100 µm zircon crystals in the rock parcel for different temperature histories presented at Fig. 11. Notice complete exponentially-accelerating dissolution of some zircon crystals and rebirth or some of them.

We have performed a series of computations targeting zircon destinies for 5,000 markers in host rocks in the growing magma body. We assume that initially rocks contain 100 ppm zirconium, that is all stored in 100 µm zircon crystals. We use Boehnke et al. (2013) zircon saturation conditions, although Watson and Harrison (1983) conditions can be easily implemented by a change of 1 line in the code if preferred; the M-factor of the melt is assumed to be a function of the temperature as suggested in Bindeman and Melnik (2016). We start simulations when the melt fraction becomes higher than 1 % and allow for change in zircon cell size caused by crystallization/dissolution of other minerals on the zircon cell's boundary. This promotes faster zircon growth during cooling, and faster zircon dissolution during country rock melting.

Fig. 12 shows the evolution of the zircon radius with time different temperature

histories presented at Fig. 11 (Q = 0.25 m^3/s and W=10 km, no eruption). As the system thermally matures progressive zircon dissolution occurs. Most of zircon cores survive until 60 ka of magma injection when significant production of eruptible melt begins (see Fig. 7, yellow curve). Most of these crystals will regrow in the same magma parcel only after 300-400 ka after the end of magma injection period. At the same time, zircons in the periphery of the melting zone that survived, complete dissolution and start to recover as the rock parcels are shifting to the colder periphery of the growing magma body.

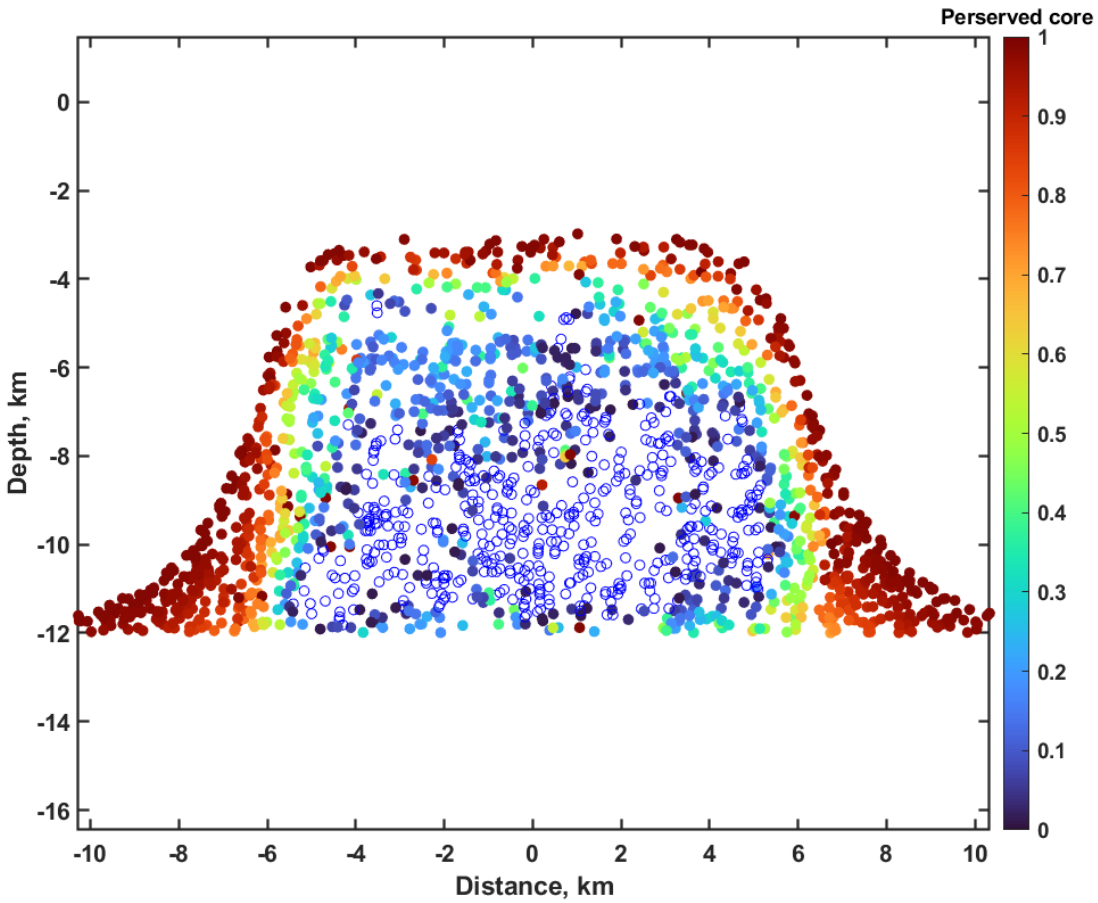

Figure 13. Fraction of preserved zircon cores for the case of system evolution with Q = 0.25 m^3/s and W=10 km, no eruption. Note predominant preservation of older cores in the periphery of the growing magma body, but that resetting zircon ages is heterogeneous in the center.

Fig. 13 shows the fraction of preserved zircon cores at final locations of 5,000 rock parcels. Unfilled markers represent completely dissolved zircons. We did not plot parcels which never experience at list 1 % melting. In the center of the injection domain only a few zircons survived complete dissolution. There is a wide halo around it that contains a mix of zircons with variably preserved cores. Due to random position of dikes, there is a significant heterogeneity at dike-to-sill transition region where the magma is introduced to colder rocks and some of them never gets significantly molten.

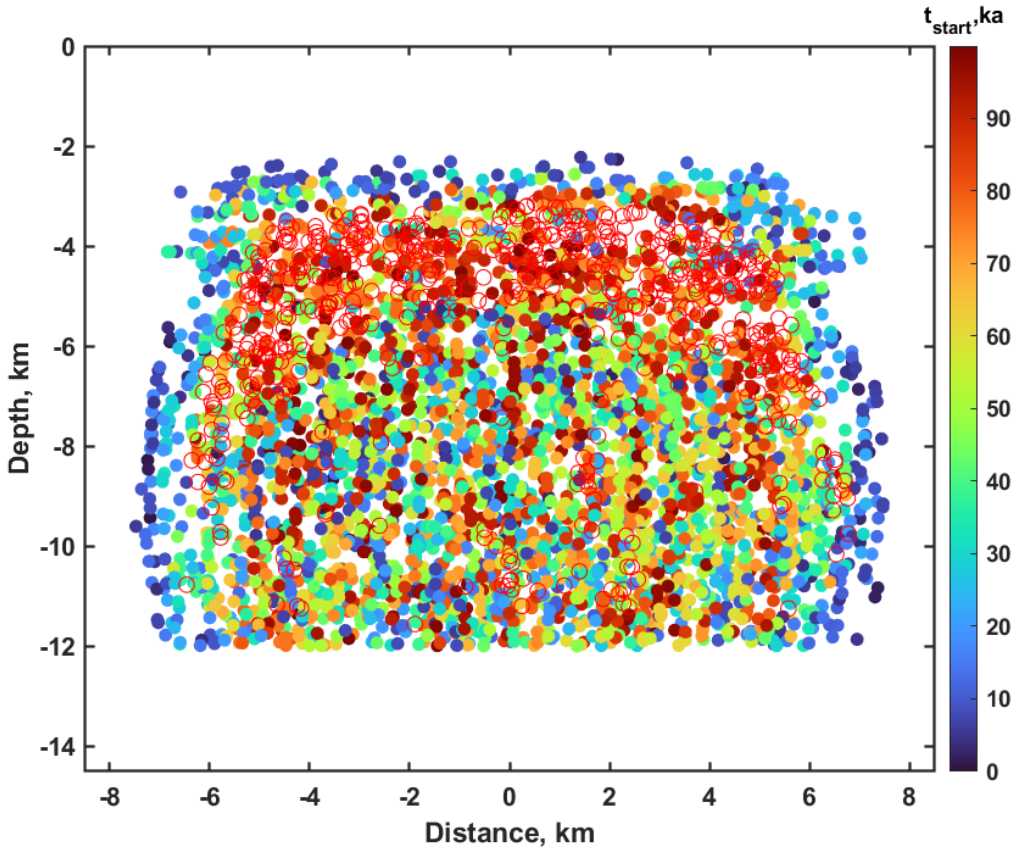

Figure. 14. Distribution of starting growth time of individual magmatic zircons for the case of system evolution with Q = 0.25 m^3/s and W=10 km, no eruption

Fig. 14 shows distribution of starting growth time for 5000 individual magmatic zircons. Opened symbols represent complete dissolution of zircons during magma injection period. These zircons will regrow later when the system starts to cool. There is a wide variety of magmatic zircon ages representing prolonged period of magma injection. Crystals start to grow as soon as injected magma cools down to Zr saturation temperatures, and often survive consequent injec-

tion of magma and preserve the core that was formed soon after the batch of magma was intruded into host rocks. In the periphery of the system dikes cool down quickly and remain cold during the formation of the magma body as they move further away from the injection region. These dikes preserve oldest magmatic zircons.

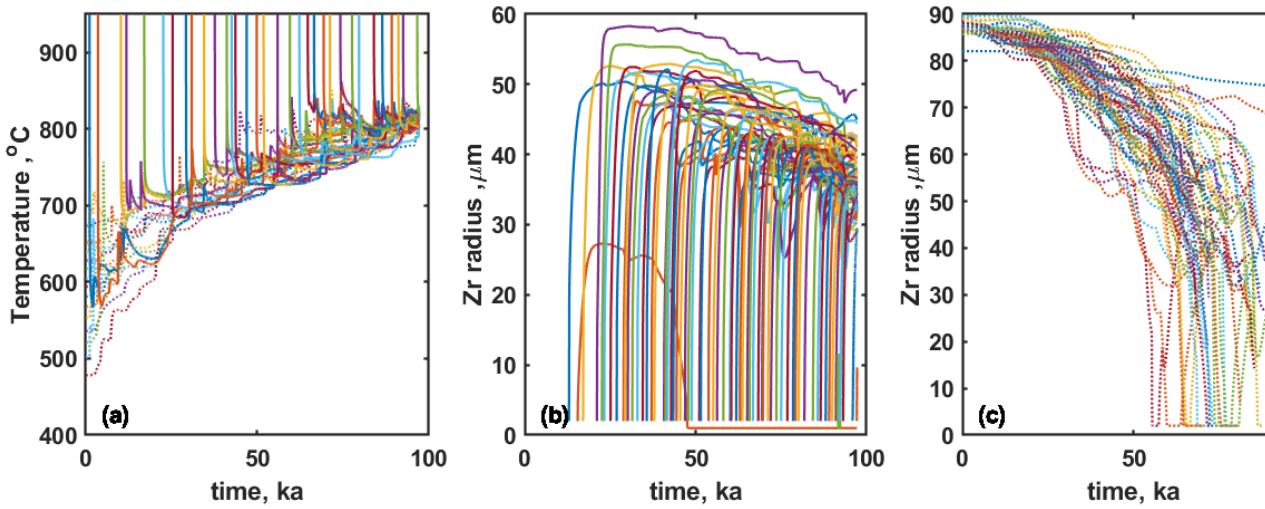

Figure 15. Temperature history of the last eruptive episode (a), growth of magmatic (b) and dissolution of host rock zircons (c). for the case of system evolution with Q = 0.25 m^3/s and W=10 km.

During the sequence of eruptions, a mixture of magmatic and host rock zircons is excavated from the reservoir. Percentage of a assimilated host rocks in eruptive products increases from 24 % to ~ 31 % as the system thermally matures (see Fig. S6). Thermal histories of magma batches are similar among different eruptions (see Fig. S7). Fig. 15a shows temperature variation in dikes (solid line) and host rock (dotted line) for the last eruption shown on Fig. 8, blue line. Dikes start at injection temperature and rapidly cool down during heat transfer with host rocks, then the temperature starts to increase with several spikes as more and more magma is introduced into the system. Later dikes experience less cooling. The eruptive temperature in ~ 820 °C corresponding to 58 % of melt in the batch. Initial dike emplacement and consequent cooling leads to the rapid growth of magmatic zircons within 1-3 ka period after zircon saturation is reached. Later on the size of crystals slowly decreases with some periods of rapid dissolution and regrowth.

Host rocks temperatures also tend towards eruptive temperature with several spikes that can dramatically increase the temperature and the degree of melting which is critical for zircon survival. Many zircons dissolve completely while others keep less than 10-20 % of its original volume (see Fig. S8). That means that the population of zircons in eruptive products will be mostly represented

by young magmatic zircons with a few percent of old resorbed cores related to host rocks.

4 Discussion

Formation of crustal magmatic systems involves magma injection from depth, heat and mass transfer, melt and gas separation and commonly episodic volcanic eruption (e.g., McBirney, 2006). No single model can capture the full complexity of these diverse processes, which would require simultaneously solving a conjugate fluid-solid-heat problem coupled with and chemical problem (phase diagram, rock compositions). Previously widely applied 1D or 2D cylindrical magma chambers models with underplating (Annen and Sparks, 2002; Dufek and Bergantz, 2005; Annen et al. 2006, Caricchi et al. 2014; 2016; Thierney et al. 2016) lead to the development of quantitative intuition of our understanding of the relationship of the magma flux rates and melting efficiencies at different geotherms and depths. In all current models, simple kinematics are prescribed, as the whole crustal column with previously intruded sills is moving vertically down upon emplacement of each additional sill intrusion, or horizontally sideways upon intrusion of a dike.

These widely utilized models of magma body formation that rely on axisymmetric geometries of intrusion with prescribed positions for magma injections and rock associated displacements provided important first-order trends in magma body formation and evolution. The model and software presented in this paper a new distributed kinematic model of 2D magma chamber formation by dike and sill injection. This allows us and potential users to investigate spatio-temporal details of magma body growth and evolution, including zircon histories. We simulated the elastic response of the country rocks to dike and sill injection, realized via spreading of markers which creates accommodation for new intrusions by moving them apart. This makes a noticeable difference in the evolution of the temperature field, melt production, and melt distribution (Fig. 3). We believe that our model provides a more realistic and high-resolution description of temperature, composition, and melt fraction and its distribution without relying on prescribed whole-system behaviors.

After the formation of large and interconnected melt regions, thermal and compositional convection can significantly intensify heat transfer, but this process is not currently considered in this model or previously published thermal-elastic models. In nature, unmolten rock screens surrounded by magma would likely sink leading to segregation of melt, and magma in large melt fraction areas in between cohesive solid framework would flow. Instead, our model assumes possibility of dike penetration through areas that are >60% molten. Similar behavior is accepted in previously proposed models of Annen et al. (2006), Annen (2009) and Caricchi et al. (2016), especially those including intraplating and overplating. To some extent, the lack of internal segregation in these models is compensated by the possibility of internal diking, balancing the overall heat and mass balance. While this may appear as locally physically unrealistic, delivery of magma through a melt layer may instead proceed via magma

addition, magma mixing and convective advection of heat and mass. These processes have similar overall effect on the thermal evolution of the system as a whole, especially in its central fully molten part. Segregation and magma mixing processes will homogenize melt fractions and temperatures to a greater degree than is shown, while global melt fraction and temperature evolution will remain similar.

The bulleted points below outline broad implications of our new model to magma body formation in nature.

1. As expected, magma flux controls the efficiency of magma production via melt accumulation and country rock melting. Equally important is melt focusing, which depends on the width of the injection region. Magma injection with the low discharge rate, or in a wide region, can produce no eruptible melt, while significant volume of melt forms for focused dike emplacement. At higher discharge rates the melt production efficiency increases but the influence of the domain size remains significant (see Fig. 3, 7).

2. The model predicts temperature-time histories of melts formed by crystallization and partial melting of host rocks. We observe highly non-monotonic temperature distributions in space and time, especially in the beginning of magma chamber formation that corresponds to individual dike emplacements into the cold crust. Formation of a significant volume of eruptible magma later in the course buffers temperature oscillations, leading to "McBirney-type" liquid core magma body (see Fig. 11).

3. Depending on the magma flux, melt focusing generates fully molten cores filled with liquidus magma and surrounded by thick "mushified" rinds and partial melt as predicted for "classic" drawings of textbook magma chambers (McBirney, 2006; Marsh, 1981). Defocused systems, and systems with low flux, generate much less melt and such systems may cool as plutons (e.g., Glazner et al. 2004), and subsequently exhibit a variety of observed intraplutonic processes of mass-redistribution (Bartley et al. 2020). The initial stages of these intraplutonic processes can be understood via our model of randomized dike intrusion (see Fig. 3,4).

4. Magma flux rates comparable to those observed in island arcs are capable of rapid generation of large, 10^3 km^3 volumes of silicic melt over ~100 ka, especially if this magma injection is focused in a relatively narrow zone, and mostly due to accumulation of such melts (see Fig 3, 7).

5. The magma system an interconnected network of dikes, sills and magma bodies over large vertical domains in the crust. Such systems are able to provide high silicic magmas discharge rates in the course of supervolcanic eruptions (Sparks et al. 2017) or voluminous Yellowstone lava flows (Loewen et al. 2017).

6. Mapping of zones of melt with >50% melt in the model demonstrates that

these are distributed in a tortuous pattern with a great deal of both vertical and lateral interconnectivity. Consequent melt migration will cause observed sample-scale heterogeneities in erupted products.

7. Magmatic systems with eruptions (Figs. 8-10) generate less overall melt than systems without eruptions because eruptions remove the hottest material to the surface.

8. Melting by basalts is more efficient than by rhyolitic magma injection. Basaltic magma melts and assimilates significantly more host rocks but remains strongly solidified itself producing high silica residual melts (see Figs. 5,7).

Our new model is tested for its ability to generate crustal melt and it describes melt volume-time histories of such melts during the growth of the intrusion and its subsequent cooling. Points below outline specific implications for our model with respect to crustal melting.

1. An important and previously unexplored result is in our 2D model is that simulated rock spreading and heat propagation leads to less efficient crustal melting. During the initial stages of intrusion (crustal preconditioning) magma is capable of melting only up to 15-20% of the granitic host crust. Subsequent intrusion will have to melt this already diluted crust-dike mixtures. Furthermore, after the establishment of the mushy rind zone with 30% crustal melt, subsequent magmatism is dominated chemically and isotopically by the intruded dikes. This result is in line with observations that even in the hot-spot related examples of magmatism, such as Iceland or the Snake River Plain, where high temperature mantle-derived Yellowstone-plume magmas intrude the Archean crust, they assimilate at most 10-20% of such crust based on Nd-crustal index (Nash et al. 2006), and based on earlier reported results of crust-wide thermomechanical modeling (e.g. Colón et al. 2019). Therefore, the high-resolution model in this paper provides a more realistic estimates of maximum possible extent of crustal melting by dike and sills intrusion.

2. We revise downward the maximum possible "melting efficiency" from previously published models, even though our model includes hot liquidus magmas. The presence of high-degree or pure crustal melts in the geologic record, commonly with a highly peraluminous nature (Bucholz et al. 2018) negates their generation by dike intrusion and implies that must be related to radioactive heating (migmatization and assembly) at deep crustal zones related to crustal thickening and burial.

3. The model also predicts lateral and vertical heterogeneities, due to naturally-generated crustal melts vs newly injected melt, for both the rhyolitic and andesitic intrusion cases. It identifies areas with >50% melt, which we interpret as eruptible magma, which contain variable proportions of crustal melt vs intruded melt. In nature this would correspond to a) varying isotopic composition, b) variable proportion of

inherited zircons, and c) in the case of basaltic partial melt-silicic remelt, various bulk melt compositions.

4. Systems with eruptions further decrease melting and crustal melting efficiencies, by as much as a factor of two. Frequent small eruptions remove heat from the system more efficiently than rare large eruptions; the latter also get higher proportion of crustal melt.

5. Integration of computed thermal and melting histories with zircon crystallization software allows us to predict zircon dissolution/crystallization conditions in 10,000 markers across the model (Fig. 11) and the dissolution/overgrowth destinies of inherited zircons. Such modeling helps in understanding zircon record in magmatic rocks that range from extremely diverse to extremely homogeneous with respect to age and isotopic values (Bindeman and Simakin, 2014; Wotzlaw et al. 2014, 2015) Fig 12-13).

6. Our on-going effort (Melnik et al. 2021 in prep) targets zircon evolution: zircon O and Hf isotopic values, trace elemental concentration in a series of magmatic systems described in this work.

Acknowledgments, Samples, and Data

This paper is dedicated to Alexander R. McBirney (1924-2019) a prominent volcanologist and a founder of the University of Oregon Volcanology Program, the first in the country. IB and OM thank RNF Grant (grant RNF19-17-00241) for support, IU thanks RFBR Grant #18-01-00352 for partial financial support, Meredith Townsend and Mike Hudak for pre-review comments. This paper is a theoretical work and does not contain new data. Executable file, example, user manual and selected temperature histories from Fig. 8 are available from the repository Melnik, Oleg; Utkin, Ivan ; Bindeman, llya (2020), "Supplementary material for JGR paper "Magma chamber formation by dike accretion and crustal melting: 2D thermal model with emphasis on zircon record"", Mendeley Data, V1, doi: 10.17632/88jmjgj7zy.1.

References

Annen, C. (2009). From plutons to magma chambers: Thermal constraints on the accumulation of eruptible silicic magma in the upper crust. Earth and Planetary Science Letters. https://doi.org/10.1016/j.epsl.2009.05.006

Annen, C., & Sparks, R. S. J. (2002). Effects of repetitive emplacement of basaltic intrusions on thermal evolution and melt generation in the crust. *Earth and Planetary Science Letters*, *203*(3-4), 937-955. https://doi.org/10.1016/S0012-821X(02)00929-9

Annen, C., Blundy, J.D., Sparks, R. S. J. (2006) The genesis of intermediate and silicic magmas in deep crustal hot zones. Journal of Petrology 47 (3), 505-539

Andrews, B. J., & Befus, K. S. (2020). Supersaturation Nucleation and Growth of Plagioclase: a numerical model of decompression-induced crystallization.

Contributions to Mineralogy and Petrology. https://doi.org/10.1007/s00410-020-1660-9

Bachmann, O., Dungan, M. A. & Lipman, P. W. (2002). The Fish Canyon magma body, San Juan volcanic field, Colorado: Rejuvenation and eruption of an upper crustal batholith. Journal of Petrology 43, 1469–1503.

Barnett, Z. A., & Gudmundsson, A. (2014). Numerical modelling of dikes deflected into sills to form a magma chamber. *Journal of Volcanology and Geothermal Research*. https://doi.org/10.1016/j.jvolgeores.2014.05.018

Bartley, J. M., Glazner, A. F., Stearns, M. A., & Coleman, D. S. (2020). The granite aqueduct and autometamorphism of plutons. *Geosciences (Switzerland)*. https://doi.org/10.3390/geosciences10040136

Becerril, L., Galindo, I., Gudmundsson, A. et al. (2013) Depth of origin of magma in eruptions. Sci Rep 3, 2762. https://doi.org/10.1038/srep02762

Biggs, J., & Annen, C. (2019). The lateral growth and coalesence of magma systems. *Philosophical Transactions of the Royal Society A: Mathematical, Physical and Engineering Sciences*. https://doi.org/10.1098/rsta.2018.0005

Bindeman, I. N., & Melnik, O. E. (2016). Zircon survival, rebirth and recycling during crustal melting, magma crystallization, and mixing based on numerical modelling. *Journal of Petrology*. https://doi.org/10.1093/petrology/egw013

Bindeman I.N., Simakin, A.G. (2014) Rhyolites—Hard to produce, but easy to recycle and sequester: Integrating microgeochemical observations and numerical models. Geosphere 10 (5), 930-957

Bindeman, I.N., Greber, N.D., Melnik, O.E., Artyomova, A.S., Utkin, I.S., Karlstrom, L., Colon,

D.P. (2020) Pervasive Hydrothermal events Associated with Large igneous provinces Documented by the Columbia River Basaltic province. *Nature Sci. Rep* 10 (1), 1-9

Brackbill, J. U., & Ruppel, H. M. (1986). FLIP: A method for adaptively zoned, particle-in-cell calculations of fluid flows in two dimensions. *Journal of Computational physics*, *65*(2), 314-343. https://doi.org/10.1016/0021-9991(86)90211-1

Bryan, S., Ernst R, (2007). Proposed Revision to Large Igneous Province Classification. Earth-Science Reviews. 86 (1): 175–202.

Bucholz, C. E., Stolper, E. M., Eiler, J. M., & Breaks, F. W. (2018). A comparison of oxygen fugacities of strongly peraluminous granites across the Archean–Proterozoic boundary. *Journal of Petrology*, *59*(11), 2123-2156. https://doi.org/10.1093/petrology/egy091

Caricchi, L., Annen, C., Blundy, J., Simpson, G., & Pinel, V. (2014). Frequency and magnitude of volcanic eruptions controlled by magma injection and buoyancy. *Nature Geoscience*. https://doi.org/10.1038/ngeo2041

Caricchi, L., Simpson, G., & Schaltegger, U. (2014). Zircons reveal magma fluxes in the Earth' s crust. *Nature*. https://doi.org/10.1038/nature13532

Caricchi, L., Simpson, G., & Schaltegger, U. (2016). Estimates of volume and magma input in crustal magmatic systems from zircon geochronology: The effect of modeling assumptions and system variables. *Frontiers in Earth Science*. https://doi.org/10.3389/feart.2016.00048

Cashman, K. V., Sparks, R. S. J., & Blundy, J. D. (2017). Vertically extensive and unstable magmatic systems: A unified view of igneous processes. *Science*. https://doi.org/10.1126/science.aag3055

Claiborne, L. L., Miller, C. F., Gualda, G. A., Carley, T. L., Covey, A. K., Wooden, J. L., & Fleming, M. A. (2018). Zircon as magma monitor: Robust, temperature-dependent partition coefficients from glass and zircon surface and rim measurements from natural systems. *Microstructural geochronology: Planetary records down to atom scale*, 1-33. https://doi.org/10.1002/9781119227250.ch1

Claiborne, L. L., Miller, C. F., Flanagan, D. M., Clynne, M. A., & Wooden, J. L. (2010). Zircon reveals protracted magma storage and recycling beneath Mount St. Helens. Geology. https://doi.org/10.1130/G31285.1

Claiborne, L. L., Miller, C. F., & Wooden, J. L. (2010b). Trace element composition of igneous zircon: a thermal and compositional record of the accumulation and evolution of a large silicic batholith, Spirit Mountain, Nevada. *Contributions to Mineralogy and Petrology*, *160*(4), 511-531. https://doi.org/10.1007/s00410-010-0491-5

Colón D.P., Bindeman I.N., Gerya T.V. (2019) Understanding the isotopic and chemical evolution of Yellowstone hot spot magmatism using magmatic-thermomechanical modeling. Journal of Volcanology and Geothermal Research 370, 13-30

Colón D.P., Bindeman I.N., Gerya T.V. (2018) Thermomechanical modeling of the formation of a multilevel, crustal-scale magmatic system by the Yellowstone plume. Geophysical Research Letters 45 (9), 3873-3879

Costa, F., Dohmen, R., Chakraborty, S. (2008) Time scales of magmatic processes from modeling the zoning patterns of crystals. Reviews in Mineralogy and Geochemistry 69 (1), 545-594

Crowley, J. L., Schoene, B., & Bowring, S. A. (2007). U-Pb dating of zircon in the Bishop Tuff at the millennial scale. *Geology*, *35*(12), 1123-1126. https://doi.org/10.1130/G24017A.1

DePaolo, D.J., Harrison, T.M., Wielicki, M., Zhao, Z., Zhu, D.C., Zhang, H, Mo, X. (2019) Geochemical evidence for thin syn-collision crust and major crustal thickening between 45 and 32 Ma at the southern margin of Tibet. Gondwana Research 73, 123-135.

Dufek, J., & Bergantz, G. W. (2005). Lower crustal magma genesis and preservation: a stochastic framework for the evaluation of basalt–crust interaction. *Journal of Petrology*, *46*(11), 2167-2195. https://doi.org/10.1093/petrology/egi049

Edmonds M., Cashman K.V., Holness M., Jackson M. (2019) Architecture and dynamics of magma reservoirs. *Philosophical Transactions of the Royal Society A Mathematical, Physical and Engineering Sciences*. 377(2139):20180298. https://doi.org/10.1098/rsta.2018.0298

Elsworth, D., Foroozan, R., Taron, J., Mattioli, G. S., & Voight, B. (2014). Geodetic imaging of magma migration at Soufrière Hills Volcano 1995 to 2008. *Geological Society, London, Memoirs*, *39*(1), 219-227. https://doi.org/10.1144/M39.12

Gerya, T.V., Yuen, D.A., 2003. Characteristics-based marker-in-cell method with conservative finite-differences schemes for modeling geological flows with strongly variable transport properties. Phys. Earth Planet. Inter. 140, 293–318. https://doi.org/ 10.1016/j.pepi.2003.09.006.

Glazner A.F., Bartley J.M., Coleman D.S., Gray W., Taylor R.Z. (2004) Are plutons assembled over millions of years by amalgamation from small magma chambers? GSA today 14 (4/5), 4-12

Gudmundsson, A., Lecoeur, N., Mohajeri, N., & Thordarson, T. (2014). Dike emplacement at Bardarbunga, Iceland, induces unusual stress changes, caldera deformation, and earthquakes. *Bulletin of Volcanology*, *76*(10), 869. https://doi.org/10.1007/s00445-014-0869-8

Heath, B.A., Hooft, E.E.E., Toomey, D.R. (2018) Autocorrelation of the seismic wavefield at Newberry Volcano: Reflections from the magmatic and geothermal systems. Geophysical Research Letters 45 (5), 2311-2318

Huber, C., Parmigiani A. (2018) A physical model for three-phase compaction in silicic magma reservoirs. Journal of Geophysical Research: Solid Earth 123 (4), 2685-2705

Huber, C., Townsend, M., Degruyter, W., Bachmann, O. (2017) Optimal depth of subvolcanic magma chamber growth controlled by volatiles and crust rheology. Nature Geoscience 12 (9), 762-768

Huppert, H., & Sparks, R. S. J. (1988). The generation of granitic magmas by intrusion of basalt into continental crust. *Journal of Petrology*, *29*(3), 599-624. https://doi.org/10.1093/petrology/29.3.599

Karakas, O., Degruyter, W., Bachmann, O., & Dufek, J. (2017). Lifetime and size of shallow magma bodies controlled by crustal-scale magmatism. *Nature Geoscience*. https://doi.org/10.1038/ngeo2959

Krumbholz, M., Hieronymus, C. F., Burchardt, S., Troll, V. R., Tanner, D. C., & Friese, N. (2014). Weibull-distributed dike thickness reflects

probabilistic character of host-rock strength. *Nature Communications*. https://doi.org/10.1038/ncomms4272

Lensky, N. G., Niebo, R. W., Holloway, J. R., Lyakhovsky, V., & Navon, O. (2006). Bubble nucleation as a trigger for xenolith entrapment in mantle melts. *Earth and Planetary Science Letters*, *245*(1-2), 278-288. https://doi.org/10.1016/j.epsl.2005.11.064

Loewen, M.W., Bindeman, I.N., OE Melnik, O.E. (2017) Eruption mechanisms and short duration of large rhyolitic lava flows of Yellowstone. Earth and Planetary Science Letters 458, 80-91

Lowenstern, J. B., Smith R.B., & Hill, D. P. (2006). Monitoring super-volcanoes: Geophysical

and geochemical signals at Yellowstone and other large caldera systems. Philosophical Transactions of the Royal Society A: Mathematical, Physical and Engineering Sciences,

364(1845), 2055–2072. https://doi.org/10.1098/rsta.2006.1813

Marsh, B. D. (1981). On the crystallinity, probability of occurrence, and rheology of lava and magma. *Contributions to Mineralogy and Petrology*, *78*(1), 85-98. https://doi.org/10.1007/BF00371146

McBirney, A.R. (2006) Igneous Petrology. Jones & Bartlett Learning, 550 p

Melnik, O. E., & Bindeman, I. N. (2018). Modeling of trace elemental zoning patterns in accessory minerals with emphasis on the origin of micrometer-scale oscillatory zoning in zircon. *American Mineralogist: Journal of Earth and Planetary Materials*, *103*(3), 355-368. https://doi.org/10.2138/am-2018-6182

Menand, T., Daniels, K. A., & Benghiat, P. (2010). Dyke propagation and sill formation in a compressive tectonic environment. *Journal of Geophysical Research: Solid Earth*, *115*(B8). https://doi.org/10.1029/2009JB006791

Miller, C. F., Furbish, D. J., Walker, B. A., Claiborne, L. L., Koteas, G. C., Bleick, H. A., & Miller, J. S. (2011). Growth of plutons by incremental emplacement of sheets in crystal-rich host: Evidence from Miocene intrusions of the Colorado River region, Nevada, USA. *Tectonophysics*, *500*(1-4), 65-77. https://doi.org/10.1016/j.tecto.2009.07.011

Muskhelishvili, N. I. (1977). Basic Equations of the Plane Theory of Elasticity. In *Some Basic Problems of the Mathematical Theory of Elasticity*. https://doi.org/10.1007/978-94-017-3034-1_4

Newhall, C. A., & Dzurisin, D. (1989). Historical unrest at large calderas of the world. Journal of

Geology; (USA), 97, 5. https://www.osti.gov/biblio/6852453

Papale, P. Global time-size distribution of volcanic eruptions on Earth. Sci Rep 8, 6838 (2018). https://doi.org/10.1038/s41598-018-25286-y

Patankar, S. (1980). Numerical Heat Transfer and Fluid Flow. Boca Raton: CRC Press, https://doi.org/10.1201/9781482234213

Robinson, J. E., & Eakins, B. W. (2006). Calculated volumes of individual shield volcanoes at the young end of the Hawaiian Ridge. *Journal of Volcanology and Geothermal Research*. https://doi.org/10.1016/j.jvolgeores.2005.07.033

Rubin, A. M. (1995). Propagation of magma-filled cracks. *Annual Review of Earth & Planetary Sciences*. https://doi.org/10.1146/annurev.ea.23.050195.001443

Schöpa, A., Annen, C., Dilles, J. H., Sparks, R. S. J., & Blundy, J. D. (2017). Magma emplacement rates and porphyry copper deposits: Thermal modeling of the yerington batholith, Nevada. *Economic Geology*. https://doi.org/10.5382/econgeo.2017.4525

Schaltegger, U., Nowak, A., Ulianov, A., Fisher, C. M., Gerdes, A., Spikings, R. et al. (2019). Zircon Petrochronology and $^{40}Ar/^{39}Ar$ Thermochronology of the Adamello Intrusive Suite, N. Italy: Monitoring the Growth and Decay of an Incrementally Assembled Magmatic System. *Journal of Petrology*, *60*(4), 701-722. https://doi.org/10.1093/petrology/egz010

Simakin, A.G., IN Bindeman, I.N. (2012) Remelting in caldera and rift environments and the genesis of hot,"recycled" rhyolites. *Earth Planet Sci Lett, 337–338*, 224-235

Simakin, A., & Talbot, C. (2001). Tectonic pumping of pervasive granitic melts. *Tectonophysics*, *332*(4), 387-402. https://doi.org/10.1016/S0040-1951(00)00297-3

Sylvester, P. J. (1998). Post-collisional strongly peraluminous granites. *Lithos*, *45*(1-4), 29-44. https://doi.org/10.1016/S0024-4937(98)00024-3

Szymanowski, D., Wotzlaw, J. F., Ellis, B. S., Bachmann, O., Guillong, M., & Von Quadt, A. (2017). Protracted near-solidus storage and pre-eruptive rejuvenation of large magma reservoirs. *Nature Geoscience*. https://doi.org/10.1038/ngeo3020

Thomson, K. (2007). Determining magma flow in sills, dykes and laccoliths and their implications for sill emplacement mechanisms. *Bulletin of Volcanology*, *70*(2), 183-201. https://doi.org/10.1007/s00445-007-0131-8

Townsend, M.R., Pollard, D.D., Smith, R.P. (2017) Mechanical models for dikes: a third school of thought. Tectonophysics 703, 98-118

Thordarson, T., & Self, S. (2003). Atmospheric and environmental effects of the 1783–1784 Laki eruption: A review and reassessment. *Journal of Geophysical Research: Atmospheres*, *108*(D1), AAC-7. https://doi.org/10.1029/2001JD002042

Walker, G. P. L. (1989). Gravitational (Density) controls on volcanism, magma chambers and intrusions. *Australian Journal of Earth Sciences*. https://doi.org/10.1080/08120098908729479

Watson, E.B. and Harrison, T.M. (1983) Zircon saturation revisited: temperature and compositional effects in a variety of crustal magma types. Earth and Planetary Science Letters, 64, 295-304.

Wotzlaw, J. F., Bindeman, I. N., Stern, R. A., D'Abzac, F. X., & Schaltegger, U. (2015). Rapid heterogeneous assembly of multiple magma reservoirs prior to Yellowstone supereruptions. *Scientific reports*, *5*, 14026. https://doi.org/10.1038/srep14026

Wotzlaw, J. F., Bindeman, I. N., Watts, K. E., Schmitt, A. K., Caricchi, L., & Schaltegger, U. (2014). Linking rapid magma reservoir assembly and eruption trigger mechanisms at evolved Yellowstone-type supervolcanoes. *Geology*, *42*(9), 807-810. https://doi.org/10.1130/G35979.1

Wotzlaw, J. F., Schaltegger, U., Frick, D. A., Dungan, M. A., Gerdes, A., & Günther, D. (2013). Tracking the evolution of large-volume silicic magma reservoirs from assembly to supereruption. *Geology*, *41*(8), 867-870. https://doi.org/10.1130/G34366.1

Zhan, Y., Gregg, P. M., Le Mével, H., Miller, C. A., & Cardona, C. (2019). Integrating reservoir

dynamics, crustal stress, and geophysical observations of the Laguna Del Maule magmatic system by FEM models and data assimilation. Journal of Geophysical Research: Solid Earth, 124, 13,547–13,562. https://doi.org/10.1029/2019JB018681